Journal of Geophysical Research: Planets

RESEARCH ARTICLE
10.1029/2018JE005618

Degradation of 100-m-Scale Rocky Ejecta Craters at the InSight Landing Site on Mars and Implications for Surface Processes and Erosion Rates in the Hesperian and Amazonian

J. Sweeney[1], N. H. Warner[1], V. Ganti[2,3], M. P. Golombek[4], M. P. Lamb[5], R. Fergason[6], and R. Kirk[6]

[1]Department of Geological Sciences, State University of New York College at Geneseo, Geneseo, NY, USA, [2]Department of Earth Science and Engineering, Imperial College London, South Kensington, UK, [3]Now at Department of Geography, University of California, Santa Barbara, CA, USA, [4]Jet Propulsion Laboratory, California Institute of Technology, Pasadena, CA, USA, [5]Division of Geological and Planetary Sciences, California Institute of Technology, Pasadena, CA, USA, [6]Astrogeology Science Center, U.S. Geological Survey, Flagstaff, AZ, USA

Abstract Rocky ejecta craters (RECs) at the Interior Exploration using Seismic Investigations, Geodesy and Heat Transport (InSight) landing site on Elysium Planitia, Mars, provide constraints on crater modification and rates for the Hesperian and Amazonian. The RECs are between 10 m and 1.2 km in diameter and exhibit five classes of preservation. Class 1 represents pristine craters with sharp rims and abundant ejected rocks. From Classes 2 to 5, rims become more subdued, craters are infilled, and the ejecta become discontinuously distributed. High-Resolution Imaging Science Experiment digital elevation models indicate a maximum depth to diameter ratio of ~0.15, which is lower than pristine models for craters of similar size. The low ratio is related to the presence of a loosely consolidated regolith and early-stage eolian infill. Rim heights have an average height to diameter ratio of ~0.03 for the most pristine class. The size-frequency distribution of RECs, plotted using cumulative and differential methods, indicates that crater classes within the diameter range of 200 m to 1.2 km are separated by ~100 to 200 Myr. Smaller craters degrade faster, with classes separated by <100 Myr. Rim erosion can be entirely modeled by nonlinear diffusional processes using the calculated timescales and a constant diffusivity of 8×10^{-7} m^2/year for craters 200 to 500 m in diameter. Diffusion models only partly capture depth-related degradation, which requires eolian infill. Depth degradation and rim erosion rates are 10^{-2} to 10^{-3} m/Myr, respectively. The rates are consistent with relatively slow modification that is typical of the last two epochs of Martian history.

Plain Language Summary The shape and form of impact craters on Mars can tell us something about processes that operate on the surface and therefore inform our understanding of the planet's climate. Small, 100-m-scale craters have a known bowl-shaped form in their pristine state. Over time, wind, gravity, and, in some cases, ice and water, degrade them to nearly flat landforms. This study analyzes the degradational sequence of craters at the InSight landing site to infer something about surface processes and climate history at this location. InSight is a geophysical mission that is set to land on Elysium Planitia in November 2018. The craters show a broad range of morphologies that suggest slow, long-term degradation. The data indicate that over time, ejected rocks and crater rims disappear at rates that suggest degradation by dry processes like gravity failure and wind erosion. Furthermore, the craters also show evidence of being filled, likely by wind-driven sand. The calculated rim erosion rates and infill rates are similar to other landing sites on Mars and suggest a cold, hyperarid climate. This is consistent with the age and equatorial location of the terrain, which formed well after the warmer and wetter period of Mars history.

Key Points:
- Presence of a meter-thick regolith and eolian infill results in relatively shallow, fresh craters at the InSight landing site
- Rim erosion can be modeled by diffusional processes, but diffusion only partly captures depth changes, which requires eolian infill
- Surface process rates at the InSight landing site are consistent with slow modification that is typical of last two epochs of Mars history

Supporting Information:
- Supporting Information S1
- Data Set S1

Correspondence to:
N. H. Warner,
warner@geneseo.edu

Citation:
Sweeney, J., Warner, N. H., Ganti, V., Golombek, M. P., Lamb, M. P., Fergason, R., & Kirk, R. (2018). Degradation of 100-m-scale rocky ejecta craters at the InSight landing site on Mars and implications for surface processes and erosion rates in the Hesperian and Amazonian. *Journal of Geophysical Research: Planets*, *123*, 2732–2759. https://doi.org/10.1029/2018JE005618

Received 22 MAR 2018
Accepted 29 AUG 2018
Accepted article online 8 SEP 2018
Corrected 16 NOV 2018
Published online 23 OCT 2018

This article was corrected on 16 NOV 2018. See the end of the full text for details.

Author Contributions:
Conceptualization: N. H. Warner, M. P. Golombek
Data Curation: N. H. Warner, J. Sweeney
Formal Analysis: J. Sweeney, N. H. Warner, V. Ganti, M. P. Golombek
Investigation: J. Sweeney, N. H. Warner, V. Ganti, M. P. Golombek, M. P. Lamb
Methodology: N. H. Warner, J. Sweeney, V. Ganti, R. Fergason, R. Kirk
Resources: N. H. Warner, M. P. Golombek, V. Ganti, R. Fergason, R. Kirk
(continued)

1. Introduction

Because the initial morphometry of Martian impact craters is well understood (e.g., Basilevsky et al., 2014; Daubar et al., 2014; Garvin & Frawley, 1998; Garvin et al., 2003; R. J. Pike, 1974, 1977; Tornabene et al., 2018; Watters et al., 2015), measurements of depth, diameter, and rim height can be used to constrain the types and rates of surface processes involved in their degradation and thus can be used to infer past Martian climate conditions (e.g., Craddock & Howard, 2000; Golombek, Warner, et al., 2014; Warner et al., 2010). The preservation state of the global Martian crater population is, however, spatially variable due to the variety of

Validation: N. H. Warner, M. P. Golombek, V. Ganti, R. Fergason, M. P. Lamb
Visualization: N. H. Warner, J. Sweeney, V. Ganti
Writing - original draft: J. Sweeney, N. H. Warner, V. Ganti

surface processes that have occurred and the complexities in local geology and climate conditions. Furthermore, the causes and rates of crater degradation are not static but have evolved throughout the planet's history (Carr, 2006; Carr & Head, 2010; Phillips et al., 2001; Scott, 1978; Soderblom et al., 1974; Tanaka, 1986). For example, the Noachian epoch (>3.7 Ga; Hartmann, 2005; Hartmann & Neukum, 2001; Michael, 2013; Werner & Tanaka, 2011) is characterized by relatively high rates of fluvial, glacial, periglacial, volcanic, and eolian activity as well as a high cratering rate (e.g., Craddock & Howard, 2002; Craddock & Maxwell, 1993; Forsberg-Taylor et al., 2004; Golombek & Bridges, 2000; Golombek, Grant, et al., 2006; Golombek, Warner, et al., 2014; Irwin et al., 2013; Mangold et al., 2012). These processes were responsible for extensive surface modification and the highest erosion rates in Martian history. Previous studies of kilometer-scale crater degradation estimate Noachian erosion rates on the order of meters per million years, comparable to relatively slow terrestrial erosion rates that are typical of tectonically stable cratonic environments as well as more arid and semiarid climates (e.g., Carr, 1992; Craddock & Howard, 2000; Craddock et al., 1997; Golombek, Grant, et al., 2006; Golombek, Warner, et al., 2014; Marchant & Head, 2007). Near the transition from the Late Noachian to Early Hesperian (3.7–3.6 Ga), surface processes diminished in variety and intensity due to atmospheric losses and a global decrease in volcanism. Erosion rates subsequently declined rapidly (e.g., Fassett & Head, 2008; Howard, Moore, & Irwin, 2005; Howard, Moore, Irwin, & Craddock, 2005; Irwin et al., 2005, 2013). During the Hesperian and Amazonian (3.6 Ga to the present), the average erosion rates were 2 to 5 orders of magnitude slower than Noachian rates (Golombek & Bridges, 2000; Golombek, Grant, et al., 2006; Golombek, Warner, et al., 2014), although there were intervals of localized, rapid surface modification due to episodic outflow channel formation and volcanism (e.g., Greeley & Schneid, 1991; Head et al., 2002; Nelson & Greeley, 1999; Tanaka et al., 2005; Warner et al., 2009). Low erosion rates on the order of ~10^{-2} to 10^{-5} m/Myr have persisted since the Early Hesperian, allowing for the near-pristine preservation of kilometer-scale impact features (e.g., Golombek, Grant, et al., 2006).

Until recently, quantitative studies of crater degradation have been limited to kilometer-sized craters on the Moon and Mars and span large, geologically diverse regions due to the large grid size of available digital elevation models (DEMs). However, the observed degradational sequence of simple and complex kilometer-sized craters (Craddock & Howard, 2002; Craddock & Maxwell, 1993; Forsberg-Taylor et al., 2004; Irwin et al., 2013; Mangold et al., 2012), and the surface modification rates derived from their preservation relative to a pristine crater model (e.g., Garvin & Frawley, 1998; Garvin et al., 2003; Tornabene et al., 2018), may not be appropriate for smaller, <1-km-sized craters. The morphology of craters of this size is far more sensitive to both target properties (e.g., Gault et al., 1968; Mizutani et al., 1983; Moore, 1971; Robbins & Hynek, 2012) and surface modification, even during the Hesperian and Amazonian, where low erosion rates caused global obliteration of small craters (e.g., Golombek, Warner, et al., 2014; Irwin et al., 2013; Warner et al., 2015). One hundred-meter-scale craters in particular are ideal for constraining relatively recent Hesperian to Amazonian surface process rates as they are too large to have been completely obliterated over this time period but are small enough to exhibit measurable morphologic change.

Rover-based observations (e.g., Golombek & Bridges, 2000; Golombek, Crumpler, et al., 2006; Golombek, Grant, et al., 2006; Golombek, Warner, et al., 2014) have ushered in the ability to analyze small crater degradation. However, the largest database of visited craters, from the Mars Exploration Rovers *Opportunity* and *Spirit*, largely includes craters that are less than 20 m in diameter. One hundred meter-scale craters were rarely visited by the Mars Exploration Rovers due to their spatial dispersion relative to the total length and analysis area of the traverse path (Golombek, Crumpler, et al., 2006; Golombek, Grant, et al., 2006; Golombek et al., 2010; Golombek, Warner, et al., 2014). Only the 750-m-diameter Victoria crater at Meridiani Planum and the 210-m-diameter Bonneville crater on the Gusev cratered plains have been described in extensive detail (e.g., Grant et al., 2004, 2006). Few studies currently exist that track both the degradational sequence and timescales of modification for a broad data set of 100-m-scale craters.

During the landing site selection process for the Interior Exploration using Seismic Investigations, Geodesy and Heat Transport (InSight) mission, the High-Resolution Imaging Science Experiment (HiRISE) camera (~0.25 m per pixel) (McEwen et al., 2007) targeted an extensive, geologically uniform region of western Elysium Planitia that exhibits an abundance of well-preserved 10- to 100-m-scale impact features (Figure 1). There is now near complete image and selected stereo coverage of the 130-km × 27-km (99% landing probability) landing ellipse (Fergason et al., 2017; Golombek et al., 2017). Additional HiRISE images and stereopairs were acquired in regions immediately adjacent to the final landing site during the landing site

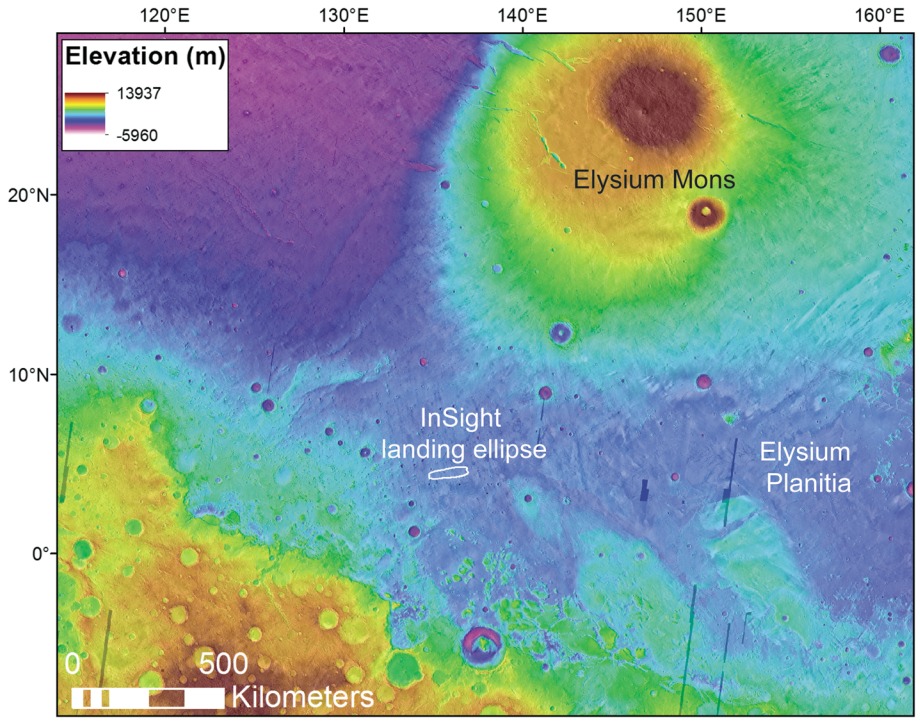

Figure 1. Mars Orbiter Laser Altimeter digital elevation model (463 m per pixel) overlain on the Thermal Emission Imaging System daytime infrared global mosaic (100 m per pixel). The location of the final landing ellipse (130 km × 27 km) for the Interior Exploration using Seismic Investigations, Geodesy and Heat Transport (InSight) mission is in white. This equatorial region, located in western Elysium Planitia, is characterized by few large impact craters and low slopes.

downselection phase, when four finalist sites were in contention (Fergason et al., 2017). This collection of HiRISE images and DEMs (Table 1) represents the largest data set for analysis of relatively small craters on any geologically uniform terrain on Mars.

Table 1
The 16 DEMs Used in This Study, the Associated HiRISE Stereo Image Pairs, and the Ellipse That Each DEM Intersects

DEM name	Image pairs	Ellipse
InSightE05_C	ESP_035996_1835; ESP_036840_1835	E5
InSightE05_FW	ESP_035139_1835; ESP_034862_1835	E5
InSightE05_W	ESP_035284_1835; ESP_035218_1835	E5
InSightE05_WC	ESP_036484_1835; ESP_037051_1835	E5
InSightE08_E	ESP_036273_1840; ESP_036207_1840	E8
InSightE08_EC	ESP_037196_1840; ESP_037473_1840	E8
InSightE08_FE	ESP_035785_1840; ESP_036062_1840	E8
InSightE08_FW	ESP_035073_1840; ESP_036550_1840	E8
InSightE08_WC	ESP_034717_1840; ESP_035561_1840	E8
InSightE09_C	ESP_038449_1845; ESP_037961_1845	E9 and E17
InSightE09_E	ESP_035640_1845; ESP_036906_1845	E9 and E17
InSightE09_EC	ESP_043183_1845; ESP_043671_1845	E9 and E17
InSightE09_W	ESP_037328_1845; ESP_037684_1845	E9 and E17
InSightE17_C	ESP_036761_1845; ESP_037262_1845	E9 and E17
InSightE17_E	ESP_034783_1850; ESP_034928_1850	E9 and E17
InSightE17_FE	ESP_036405_1850; ESP_036695_1850	E9 and E17

Note. HiRISE = High-Resolution Imaging Science Experiment; DEM = digital elevation model.

1.1. InSight Landing Site and Rocky Ejecta Craters

InSight is a geophysical mission that will examine the Martian interior in order to improve the current understanding of terrestrial planet formation (Banerdt et al., 2017). For successful landing and instrument deployment, the landing site, in addition to meeting elevation (<-2.5 km) and latitude (3–5°N) requirements, must be a relatively flat, load bearing surface with low rock abundance and possess a fragmented regolith that is 3–5 m deep for penetration of the heat flow probe (HP^3). Landing site analyses by Golombek et al. (2017) confirmed that a region of regolith-covered Early Amazonian to Hesperian-age lava plains in Elysium Planitia best accommodates these criteria (Figure 1). Geologic mapping using Mars Reconnaissance Orbiter (MRO) Context Camera (CTX) imagery at 6 m per pixel and the global Thermal Emission Imaging System daytime and nighttime mosaics at 100 m per pixel (e.g., Golombek et al., 2017; Warner et al., 2017) showed that the landing region is dominated by a single, geologically, and thermally uniform unit called Smooth Terrain. Local variations in the morphology and thermal characteristics of the Smooth Terrain unit are related to surficial processes that have etched and possibly removed only the upper few meters of the loosely consolidated regolith (e.g., Gradational, Dark, and Etched Terrains; Golombek et al., 2017). Tanaka et al. (2014) defined this region as ridged plains, part of the Early Hesperian transitional unit (eHt). The Early Hesperian age was

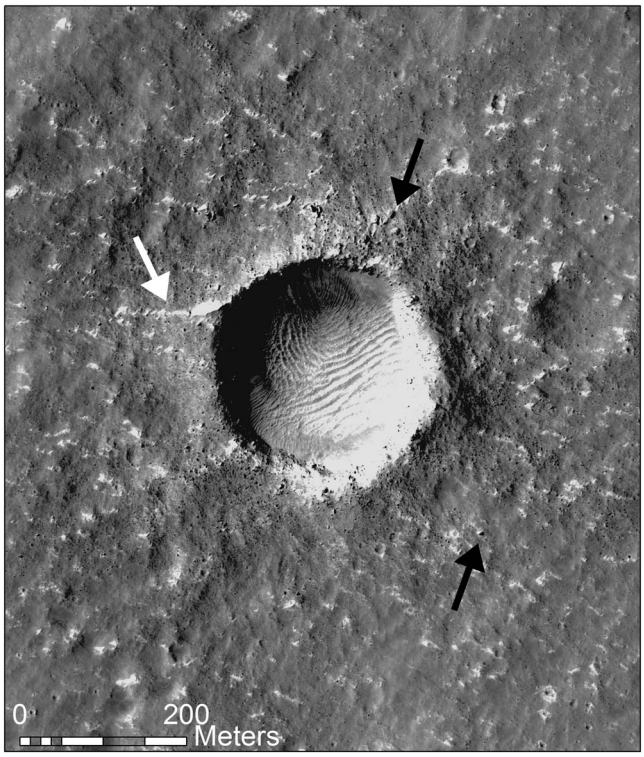

Figure 2. High-Resolution Imaging Science Experiment image (0.25 m per pixel) of a 200-m-diameter rocky ejecta crater. The fresh Class 2 crater displays a nearly continuous ejecta blanket consisting of boulder-sized rocks (black arrows show large examples) and meter-scale eolian bedforms on the crater floor and in the ejecta blanket. A relatively large bedform is trapped against the northwest rim of the crater (white arrow). Image ESP_037961_1845.

determined from crater counts that include craters ≥5 km in diameter. CTX-based crater counts, including all craters ≥200 m in diameter, suggest an Early Amazonian resurfacing event that removed or buried craters <2 km in diameter (Warner et al., 2017). The model age derived from the <2 km-diameter-population is ~1.7 Ga, which represents the maximum age of all 100-m-scale craters in the landing site.

All terrains in the landing region exhibit rocky ejecta craters (RECs; Figure 2), a relatively young group of craters that range in diameter from as small as 10 m to as large as 2 km, with the majority of RECs occurring above 30 m in diameter (Warner et al., 2017). The data set presented here includes RECs with diameters between 10 m and 1.2 km. Their youth is partly inferred by the appearance in HiRISE imagery of decimeter to meter-sized rocks within an ejecta blanket that extends approximately one crater diameter (*D*) from the crater rim (Figure 2). These ejected rocks are sourced from a more competent rocky unit that occurs at depth below the regolith. The upper stratigraphic contact of the rocky unit with the surficial regolith is as shallow as 2 to 5 m below the surface to as deep as 12 to 18 m (Warner et al., 2017). The observed lack of RECs below diameters of 30 to 50 m (a few outlier RECs do occur below 30 m) implies that the uppermost 2 to 5 m of excavated material is a loosely consolidated, granular regolith.

The purpose of the present study is to provide a detailed morphologic and morphometric analysis of RECs across the InSight landing region to evaluate processes and rates of 100-m-scale crater degradation for typical Hesperian to Amazonian-age ridged plains. The data are derived from observational analyses of available HiRISE imagery and semiautomated methods that use 3-D Analyst tools in ArcMap to measure crater morphometry from HiRISE DEMs. The data are used to (1) assess the morphometry (e.g., diameter, depth, and rim height) of craters to evaluate how a crater changes over time and the processes involved in their degradation; (2) develop a history of crater degradation using the size-frequency distribution (SFD) of RECs; (3) constrain surface erosion rates with implications for local surface processes and the climate history of Mars; and (4) compare the observed morphometric changes and rates to diffusion models that have been used previously to constrain impact crater modification (Armitage et al., 2011; Fassett & Thomson, 2014; Golombek, Warner, et al., 2014).

2. Methods: Crater Morphometry

2.1. Data Sets and Crater Mapping

Sixteen HiRISE DEMs (Table 1) at 1-m grid spacing and the associated 1-m orthorectified HiRISE images were used to identify and map 2866 RECs (Figure 3). The morphology of each crater was qualitatively described using the full-resolution ~0.25- to 0.30-m per pixel HiRISE images. The DEMs were created using an equirectangular projection. Crater depth (*d*), rim height (*h*), and diameter (*D*) were quantified using the DEMs in this projection. The DEMs, orthoimages, and full-resolution images were then coregistered to the InSight landing site CTX basemap and geologic map (Golombek et al., 2017) with a simple cylindrical projection using the georeferencing tie-pointing method in ArcMap. This coregistered map was used to visually compare the topographic characteristics of each crater to the visual characteristics (e.g., rock abundance and albedo) and mapped geologic units.

The HiRISE DEMs were created by the U.S. Geological Survey (USGS) from stereo images and the BAE SoftCopy Exploitation ToolSET (SOCET-SET) stereogrammetry program according to standard USGS methods (e.g., Kirk et al., 2008). Fergason et al. (2017) describe the methodology for constructing this set of DEMs, which were created specifically for the InSight landing site evaluation. The DEMs were subject to an unusually high level of quality control and validation by the USGS and Jet Propulsion Laboratory prior to their release. The quality control process included visual inspection of the DEMs, evaluation of derived height contours superimposed onto images, generation and comparison of DEM histogram statistics, calculation of vertical

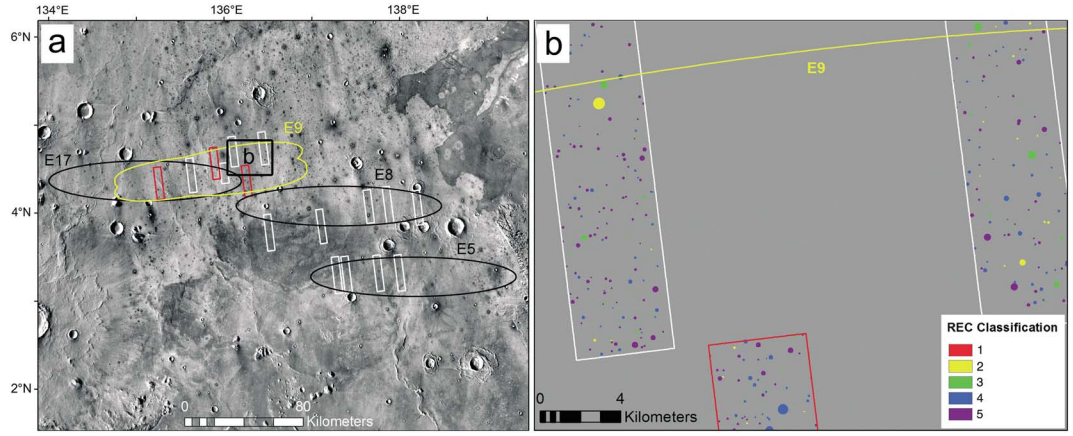

Figure 3. (a) Thermal Emission Imaging System (THEMIS) daytime infrared mosaic (100 m per pixel) of the InSight landing region. The final landing ellipse (E9) in yellow is shown as the merged open, middle and close orientations for the May 2017 launch window. Three other candidate landing ellipses E5, E8, and E17 are in black. E9 is dominated by Smooth Terrain (Golombek et al., 2017), which is noted in THEMIS by its uniform moderate thermal inertia signature. The western and southern edges of ellipses E5, E8, and E17 contain units with higher thermal inertia, noted by cooler (i.e., darker) daytime infrared signatures. The dark halo (cool daytime temperatures) around craters is representative of ejected rocks with high thermal inertia. The red boxes outline the locations of the three HiRISE DEMs used for manual measurements. The white rectangles outline the locations of the 13 additional HiRISE DEMs analyzed in this study. (b) Example mapped distribution of classified RECs in the northeast portion of E9. The color code is the classification scheme for the relative degradation states. HiRISE = High-Resolution Imaging Science Experiment; InSight = Interior Exploration using Seismic Investigations, Geodesy and Heat Transport; REC = rocky ejecta crater; DEM = digital elevation model; THEMIS = Thermal Emission Imaging System.

precision, and calculation of position accuracy (horizontal and vertical) from overlapping CTX and HiRISE DEMs (details in Fergason et al., 2017). Manual editing tools in SOCET-SET were employed to correct blunders or artifacts. Manual editing required approximately 40 hr per DEM. For the InSight DEMs, the expected vertical prevision ranges from 0.1 to 0.2 pixels. The vertical precision of the DEMs is sufficient to reveal sub-meter-scale rocks in the ejecta, bedforms on the crater floors and shallow craters superposed on the crater rims (supporting information Figure S1).

The DEMs and images cover a region within the final four InSight landing sites (E5, E8, E9, and E17) that were under consideration during landing site selection (Fergason et al., 2017; Golombek et al., 2017; Figure 3). The Smooth Terrain unit, identified throughout the landing site region (Golombek et al., 2017), covers 80% of the HiRISE coverage area. Smooth Terrain is identified by its moderate thermal inertia (~200–250 $J{\cdot}m^{-2}{\cdot}K^{-1}{\cdot}s^{-1/2}$), noted in daytime Thermal Emission Imaging System infrared images by its warmer (i.e., lighter) signature compared to neighboring terrains (Figure 3). Smooth Terrain also exhibits a moderate albedo in visible light images, low rock abundance (<5% cumulative fractional area [CFA]), and low regional and local slopes (≤4° over 2- to 5-m length scales; Golombek et al., 2017). The thermal and visible characteristics indicate that the surface is composed of cohesionless sand-sized particles or mixtures of cohesive soils, rocks, and a thin dust coating. The higher thermal inertia terrain units, noted for their relatively cool (i.e., dark) daytime infrared signature (Figure 3), also occur in the study region and include Etched Terrain, Gradational Terrain, and Dark Terrain (Golombek et al., 2017). These units occupy 15% of the study area and are confined to the southwestern portion of ellipse E8 and the western margin of E5. The higher thermal inertia at these locations is due to a higher rock abundance (<10–20% CFA) that may represent a lag of coarser materials that resulted from enhanced eolian stripping of the sand-sized component of the regolith, which is normally intact on the Smooth Terrain. Other accessory terrain units, including areas covered by clusters of 100-m-scale secondary craters, occupy the remaining area. HiRISE images reveal that the meter-scale rock abundance within the ejecta of the RECs on all terrain types is significantly higher than the background rock abundance outside of the ejecta blanket (Figure 2). In rim-proximal regions of the ejecta, the rock abundance may exceed 36% CFA (Golombek et al., 2017). This allows RECs to be mapped with relative ease in HiRISE across all terrain types.

Mapping of the RECs excluded obvious secondary craters, which were visually discerned by their occurrence in clusters and chains. Secondary craters from Corinto crater (Golombek et al., 2017; McEwen et al., 2005) in particular are ubiquitous across the landing region and are easily noted for their consistent size range

(10–50 m), bright lobate ejecta, and association with north-south trending clusters that point back to the primary crater (Golombek, Bloom, et al., 2014; Golombek et al., 2017). Randomly distributed, far-field secondaries are difficult to distinguish from primary impact craters using their morphology. Morphometric characteristics that scale with distance downrange from the source crater are useful for interpreting a secondary origin (Watters et al., 2017). However, these relationships cannot be confidently used to map random secondaries where the source crater is unknown. Contamination by random secondaries, particularly for <100-m-scale-diameter craters, is always possible in a crater mapping exercise and is even included in the derivation of the established crater production functions (e.g., Hartmann, 2005). Degraded craters that lack rocks in the ejecta were also excluded from the larger data set, although individual degraded craters were sampled using the HiRISE DEMs. The absence of rocks surrounding these deteriorated craters is attributed to the erosion and/or burial of rocks excavated by the impact. At diameters <200 m, but more typically <30 to 50 m, fresh craters may also lack rocks in the ejecta because the impacts were not large enough to access the rockier unit that occurs beneath the regolith (see discussion in Warner et al., 2017). These fresh, nonrocky ejecta craters (NRECs) were also excluded from this data set.

2.2. Classification Based on Observed Morphology

Following the mapping phase, each REC was classified based on the relative state of degradation as viewed in HiRISE imagery. The diameter of the crater was not considered in this classification. For example, a pristine 20-m crater is grouped within the same class as a 200-m pristine crater despite the likelihood that craters of different sizes degrade at different rates. The relationship between specific morphometric parameters (e.g., diameter and interior slope) and the rate of crater degradation will be discussed in later sections. The classification system includes five classes (Class 1 to Class 5), where Class 1 represents the most pristine REC and Class 5 represents the most degraded examples that still include rocks in their ejecta (Figures 4 and 5). The classification scheme was established during the landing site selection phase (see Golombek et al., 2017; Warner et al., 2017) to evaluate landing hazards associated with the RECs and to provide constraints on regolith thickness. Details of the classification system are summarized below.

Class 1 craters represent the near-pristine morphology of a simple crater and as such are rare. They are noted by a clearly defined sharp rim, no superposed craters, eolian bedforms in the ejecta blanket and well-preserved rocks within a 1*D* annulus that constitutes the continuous ejecta blanket (Figure 5). Bedforms are commonly observed within a Class 1 crater. Class 1 craters also exhibit either well-defined low albedo rays that represent a blast zone where impact-generated wind removed the higher albedo dust cover (Daubar et al., 2013) or rays of ejected basaltic material that superpose the dust.

From Class 1 to Class 5, the craters follow a continuum of degradation that includes lowering and rounding of the rim, formation of rim notches or gaps, disappearance of rocks in the ejecta blanket, migration of bedforms from the ejecta blanket to the crater interior, filling and smoothing of the crater floor, and increased presence of craters superposed on the ejecta, rim, and infill (Figure 4). This sequence of degradation occurs for all RECs in the data set at all diameters. Class 2 craters show significant accumulation of bedforms on the crater floors (Figure 4a) suggesting that time has progressed and sand-sized materials have migrated into the craters. HiRISE and CTX images of Class 2 craters show a relatively high albedo ejecta blanket in contrast to the surrounding moderate albedo plains (Figures 2 and 4a). The high albedo corresponds with the presence of meter to sub-meter-scale eolian bedforms. Class 2 craters also show a well-defined rim with some rounding and intermittent gaps, rocks in the 1*D* annulus, and an occasional superposed crater.

The transition from Class 2 to Class 3 is defined by increased degradation of the ejecta and rim and further infilling of the crater (Figures 4c and 4d). By the Class 3 stage, bedforms within the crater interior have become partially smoothed off, likely by formation of a soil with minor near surface cohesion as has been observed at many of the landing sites (Golombek et al., 2008). Yet some bedforms still remain, suggesting ongoing sand migration into the crater. Furthermore, much of the sand-sized material that was once present within the ejecta during the Class 2 stage is trapped at this stage against the exterior of the elevated crater rims. This indicates that some portion of the sediment supply to the crater interior comes directly from the sand that was initially trapped within the ejecta blanket during the Class 1 and Class 2 stages. The rims of Class 3 craters are noted for their relatively bright appearance due to these higher albedo bedforms.

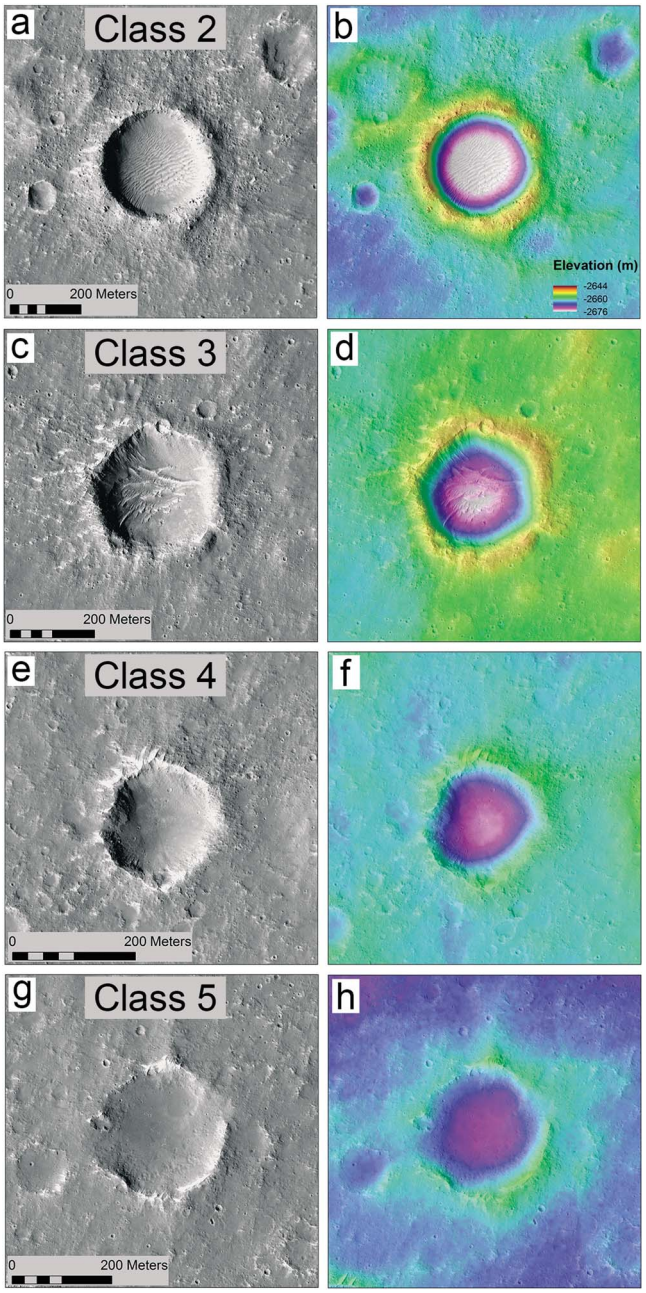

Figure 4. High-Resolution Imaging Science Experiment image ESP_037961_1845 (0.25 m per pixel) and the corresponding digital elevation model InSightE09_C (1 m) displaying the different morphologic classes of rocky ejecta craters. Crater class was determined from the morphology of the rim, floor, and ejecta (see text for classification criteria). From freshest to most degraded, the classes are (a and b) Class 2 crater, (c and d), Class 3 crater, (e and f) Class 4 crater, and (g and h) Class 5 crater.

Class 4 craters show degraded rims with more notches, gaps and rounding, intermittent coverage of the continuous ejecta blanket by ejected rocks, few bedforms preserved against the rims of the craters, and smooth infill that completely covers the crater floors (Figures 4e and 4f). Despite the infill, few interior bedforms are observed. The infill often preserves small impact structures with fairly well defined rims, indicating some induration. Small craters commonly superpose the infill.

Class 5 craters represent the most degraded crater class that still has rocks preserved in the ejecta blanket (Figures 4g and 4h). However, the rock abundance is low and the mappable areal extent of the rocky ejecta blanket is $<25\%$ of the 1D annulus. Class 5 craters still exhibit an elevated and rounded rim, although the rim circumference is dominated by gaps. The rim may still trap bedforms, yet most of the sand that was trapped by the rim at the Class 3 and 4 stages has migrated away from the crater as the rim has become less of a topographic obstacle and the interior has become less of a sediment trap. All Class 5 craters are incompletely filled. The smooth interior material retains superposed craters at the Class 5 stage.

This classification scheme excludes the more degraded craters that completely lack meter-scale rocks in the ejecta and whose rims are almost completely obliterated (Figure 6). The coupling of rim morphology to the disappearance of rocks in the ejecta suggests that the rim degrades at a similar rate to the rocks. For ease of comparison, these older craters will herein be referred to as Class 6 craters. Collectively, a Class 1 crater of some diameter is assumed to be younger than a Class 2 crater of that same diameter, which is younger than a similar-sized Class 3 crater, and so forth. This assumption is also likely valid within a diameter range/bin as long as the craters within that range degrade at similar rates and show a similar time dependence on morphology. Importantly, all of the mapped craters in this region occur on terrains with a similar age, latitude, and geologic history (Golombek et al., 2017). All RECs in the data set therefore have been modified by the same set of surface processes.

2.3. Morphometric Analysis From HiRISE DEMs

The number of RECs that occur in the study region exceeds the ability to measure their morphometry (depth [d], rim height [h], and diameter [D]) using traditional manual profiling methods. In a pilot study of the morphometry of the RECs in the InSight landing site, Sweeney et al. (2016) constructed four topographic profiles across each crater within ArcMap using three 1-m HiRISE DEMs (Figure 3). Depth measurements were taken from 516 RECs. Rim height was acquired from 199 RECs. The original manual method for calculating depth involved fitting four profiles that spanned the crater and its continuous ejecta blanket from north-south, east-west, northeast-southwest, and northwest-southeast. A mean crater depth was calculated using each 2-D transect by comparing the average rim elevation to the deepest point within the crater. Rim height was acquired from eight rim locations, comparing the rim elevation at these points to the plains elevation. The plains elevation was manually queried from the DEM at a point immediately beyond the outer edge of the continuous ejecta blanket of each crater. While these profiling methods are relatively straightforward, it is time intensive and the data are derived from only a limited set of arbitrarily drawn transects. For this new study, a faster, partially automated approach using 3-D Analyst tools in ArcMap was tested and applied to evaluate a larger set of craters that span a broader region of the InSight landing site. The following methodology details this approach.

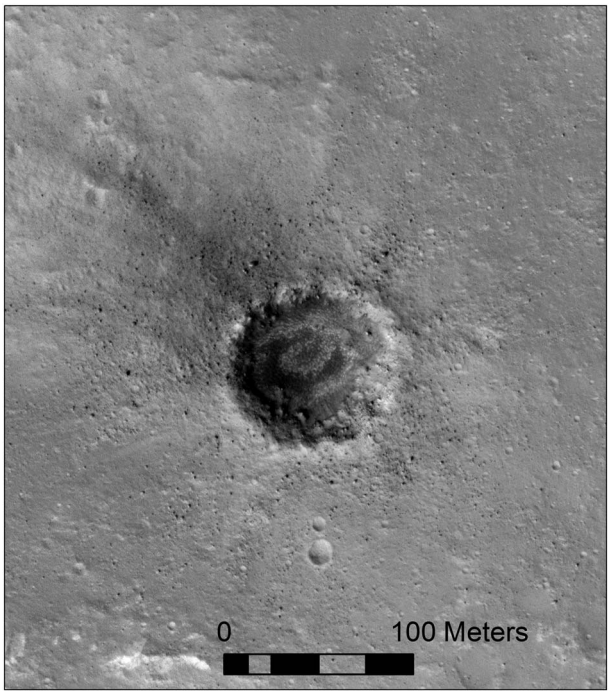

Figure 5. High-Resolution Imaging Science Experiment image of a ~70-m-diameter Class 1 rocky ejecta crater with dark interior and rocky ejecta. Image ESP_048128_1845.

2.3.1. Semiautomated Measurements

Semiautomated methods for measuring *d* and *h* were first performed on 516 and 199 RECs, respectively, corresponding with the original Sweeney et al. (2016) crater data set. This was done to test the faster ArcMap method before expansion to a larger sample of RECs. The semiautomated method requires crater shapefiles, coregistered to the HiRISE DEMs, as inputs. Crater shapefiles were constructed by two point digitization, including the center point and rim of the crater. The resultant shapefile represents the approximate rim to rim diameter, assuming a circular shape (supporting information Figure S2). While a perfect circle is obviously not entirely representative of every crater, we accept this simplification for the benefit of analysis time. Each crater was manually edited to ensure the best possible alignment between the shapefile and the rim geometry. However, the exact rim crest of a crater is difficult to precisely define and some craters, particularly those below 100 m in diameter, are not circular. Centimeter to 1-m-scale (~1 to 10 pixels) offsets occur where the edge of the circle shape does not exactly align with the rim height maxima. Depending on the crater rim width and general slope characteristics, which are dependent on the crater diameter and preservation state, this offset can result in up to 3 to 5 m of vertical error in the depth measurements for larger (>500 m) craters (supporting information Figure S2). More commonly, ≤1 m of vertical error is indicated due to rim offsets for smaller and more degraded craters.

Workflows for measuring depth and rim height from the initial shapefiles were built in the ArcMap ModelBuilder environment. This allows for the measurements to be taken from thousands of craters simultaneously. The steps for measuring depth in ArcMap are the following: (1) Convert the circular crater shapefiles to points (supporting information Figure S2a). The number of evenly spaced points per crater scales with diameter, from 37 points for the smallest 10-m craters to 175 points for the largest 1.2-km crater. (2) Add elevation data from the DEM to the points using the Add Surface Information function in ArcMap. This function adds *Z* values from the DEM using the *XY* location of each point. (3) Create a triangular irregular network (TIN) from the point elevation data. This function interpolates (linear interpolation method) a series of triangular surfaces across the crater that are pinned by the elevation of the evenly spaced rim elevation points. A TIN was chosen to represent an irregular rim to rim surface, opposed to a planar surface of equal elevation, to capture the

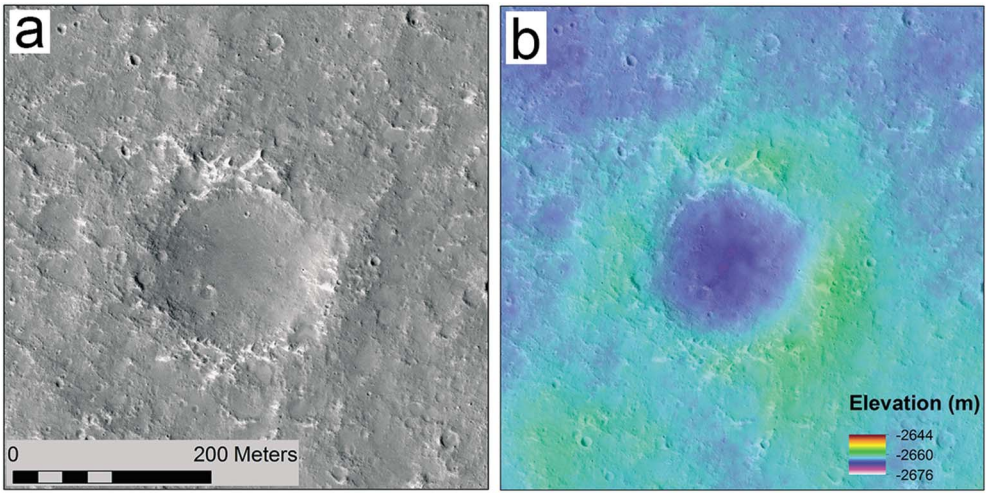

Figure 6. High-Resolution Imaging Science Experiment image ESP_037961_1845 and the corresponding digital elevation model showing a degraded Class 6 crater with a shallow, filled interior, low rim and no rocks in the ejecta blanket.

meter-scale variability in rim height. (4) Convert the TIN to raster format at 1-m grid spacing to match the underlying HiRISE DEM. This raster is an interpolated (linear interpolation method) DEM of the TIN, spanning the crater interior. (5) Subtract the underlying HiRISE DEM from the overlying rim to rim raster to isolate the depth of the crater floor below the rim elevation (supporting information Figure S2b). The maximum difference between the HiRISE DEM and the rim elevation raster is the depth of the crater. Depth is referred to throughout as a mean depth because it is a measure of the maximum difference between the DEM and the mean elevation of the crater rim, consistent with methods presented in Boyce and Garbeil (2007), Boyce, Mouginis-Mark, and Garbeil (2005), Boyce, Mouginis-Mark, Garbeil, and Soderblom (2005), Robbins and Hynek (2012), and Watters et al. (2015). Maximum and minimum depths were also determined as the maximum difference between the DEM and raster with respect to the maximum and minimum rim height values.

Before measuring rim height, a 1*D* annuli buffer shapefile was constructed extending from the outer edge of each crater shapefile (supporting information Figure S3a). The outer edge of this buffer is inferred to fully include the continuous ejecta blanket and extends to the preimpact surface. A shapefile that represents the approximate plan view width of crater rim was also initially constructed for each crater using the circular shapefiles and the buffer function in ArcMap. Because the circle shapefile may not lie exactly on the crest of the crater rim, the rim width buffer creates a polygon that generally encompasses the entire rim structure of the crater. This polygon is then used to extract the maximum, minimum, and mean elevation values of the rim from the DEM (supporting information Figure S3b). Based on topographic profile measurements of 87 fresh, 10- to 100-m-scale craters in the landing site, rim width was determined to scale with crater diameter by ~0.02*D*. Buffer shapefiles were applied to every crater using this function. With the annuli and rim buffer shapefiles, the following steps were applied to measure rim height: (1) Convert the edge of the 1*D* annuli shapefiles to points. The number of evenly spaced points per buffer scales with crater diameter, from 255 points for the smallest 10-m craters to 1,538 points for the largest 1.2-km crater. (2) Add elevation data from the HiRISE DEM to the points using the Add Surface Information function. The points record the preimpact surface plains elevation at 1*D* distance from the crater rim. (3) Create an interpolated TIN (linear interpolation method) from the point elevation data and convert the TIN to raster format with 1-m grid spacing. This raster is an interpolated DEM that approximates the elevation of the preimpact surface. (4) Subtract this interpolated raster from the HiRISE DEM to isolate the height of the crater rim above the plains. (5) Clip the resulting rim height raster to the rim width buffer shapefile. The mean rim height value is the measured mean of the resultant rim height raster, calculated 360° around the crater circumference. Maximum and minimum values were also determined.

2.3.2. Comparison of Manual and Semiautomated Measurements

While the semiautomated method introduces multiple steps of interpolation to generate an artificial rim to rim surface or preexisting landscape, it does offer a means of calculating depth and rim height for all craters on a DEM using a relatively simple string of standard ArcMap functions. Errors introduced by calculating depth and rim height from an interpolated surface are difficult to quantify for thousands of craters. There are compounding assumptions that include the choice of the exact rim/plains location, number of points available for TIN construction, and the chosen interpolation method (e.g., linear, bilinear, and natural neighbor). The results of the more standard, manual profiling method are ultimately used here as a test of the fidelity of the semiautomated approach for application to the broader crater data set. There is strong agreement between the manual and semiautomated methods for both the depth and rim height measurements for the initial data set of craters (Sweeney et al., 2016; Figures 7 and 8). The R^2 and P values, comparing depth data from each method, are 0.99 and 0, respectively (Figure 7a). The mean depths from the semiautomated method are slightly lower than, and the range for each crater larger than, the manually measured equivalents (Figures 8a and 8b). This suggests that the new method captures more of the total variability in d than the manual measurements due to the inclusion of the entire crater rim in the measurement. Troughs or gaps are present on many of the craters in the landing site and are often excluded during the manual profiling method due to the limited number of transects. The rim heights, measured from a smaller data set of 199 RECs, are also consistent between the two methods (Figure 7b). Similar to the semiautomated results for crater depth, the new ranges in rim height are greater than the manual ranges (Figures 8c and 8d). The semiautomated method provides a less biased representation of crater rim height variability.

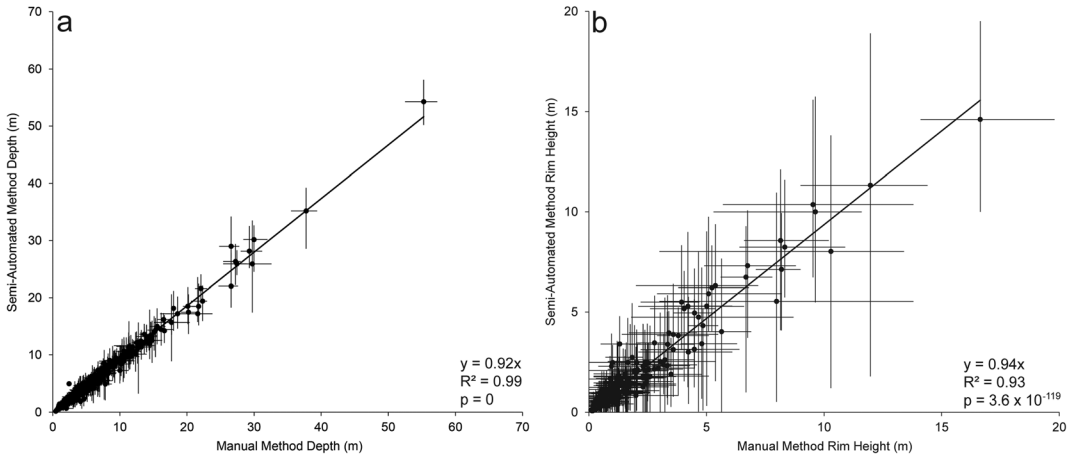

Figure 7. (a) Comparison of crater depth determined from the manual profiling method (*x* axis) and the semiautomated method (*y* axis). (b) Comparison of manually measured (*x* axis) crater rim heights and semiautomated (*y* axis) rim heights. Data are derived from three High-Resolution Imaging Science Experiment digital elevation models. Whiskers represent the maximum and minimum values of each measurement.

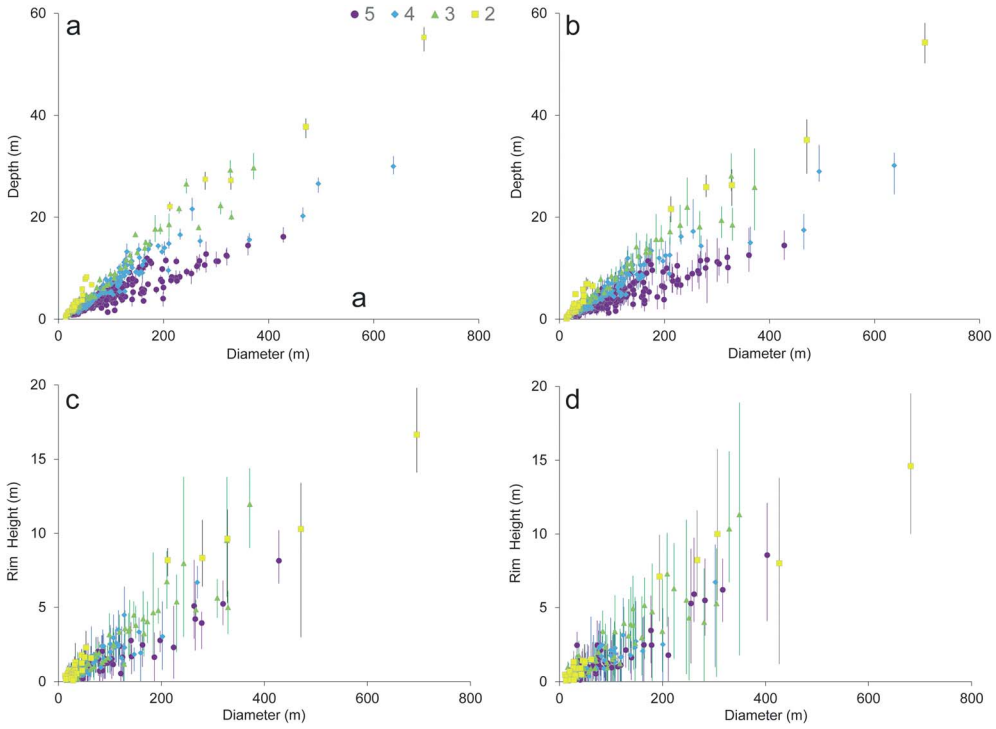

Figure 8. Crater depth and rim height as a function of diameter separated by crater class for a set of 516 and 199 craters, respectively. Data derived from three High-Resolution Imaging Science Experiment digital elevation models. Symbols and colors relate to the morphometric classification system. Whiskers show the minimum and maximum values for each crater. (a) Linear plot showing the manually measured crater depths. The maximum and minimum depth values were determined directly from crater profiles. (b) Linear plot showing crater depths as measured by the semiautomated method. The maximum and minimum values were determined by subtracting the lowest point on the floor of the crater from the minimum and maximum rim elevation values. (c) Linear plot showing the manually measured crater rim heights. Maximum and minimum values were determined directly from the crater profiles. (d) Linear plot showing crater depths as measured by the semiautomated method. Maximum and minimum values were determined from subtracting the plains elevation from the maximum and minimum elevation values of the rim. The ranges indicate that there are significant topographic gaps in the rim. In many cases, this provides a near-zero height minima. Class 1 craters not shown due to limited digital elevation model coverage.

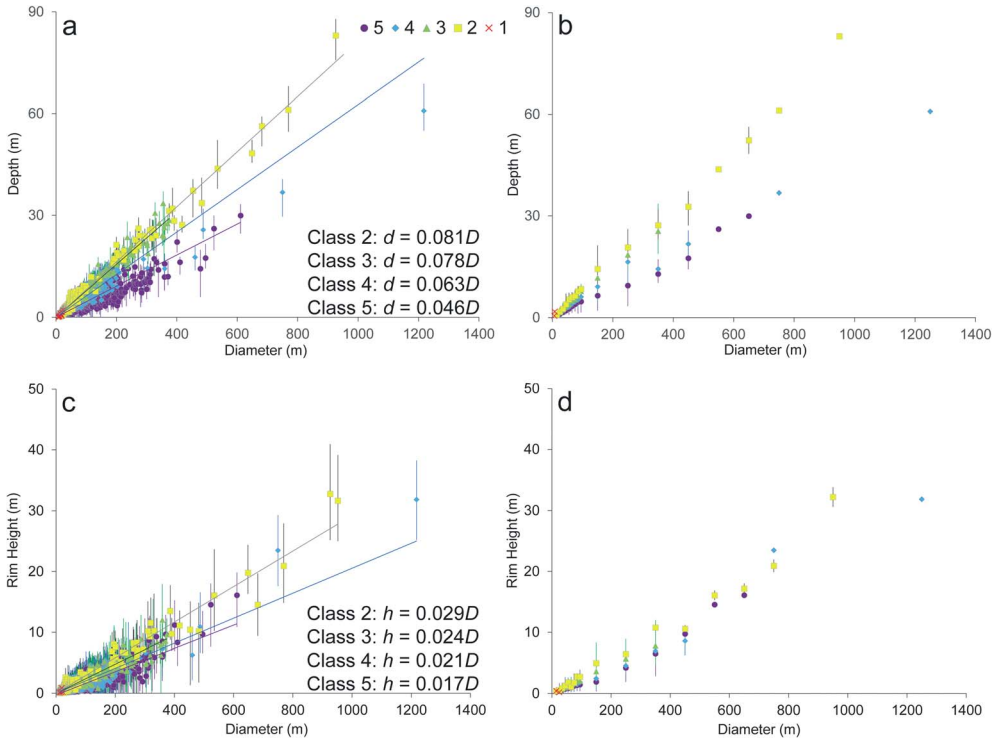

Figure 9. Morphometric results relating mean crater depth d and rim height (*h*) to crater diameter (*D*) from semiautomatic processing for the entire rocky ejecta crater data set including 2,866 craters for the depth data set and 2,725 craters for the rim height data set. (a) Linear plot of unbinned *d*/*D* data. (b) Linear plot of binned *d*/*D* data provided for clarity (pseudolog binning). (c) Whiskers show the minimum and maximum depth for each crater. Maximum and minimum values in the unbinned data were determined by subtracting the lowest point on the floor of the crater from the minimum and maximum rim elevation values. Whiskers for binned data show the range of mean crater depths in each diameter bin. (c) Linear plot of unbinned *h*/*D* data. (d) Linear plot of binned (pseudolog) *h*/*D* data provided for clarity. Maximum and minimum values for the unbinned data were determined from subtracting the plains elevation from the maximum and minimum elevation values of the rim. The ranges indicate that there are significant topographic gaps in the rim. In many cases, this provides a near-zero height minima. Whiskers for binned data show the range of mean crater rim heights in each diameter bin. Symbols and colors relate to the morphometric classification system.

3. REC Morphometry Results and Comparison to Observed Degradation State

The semiautomated method was applied to the large data set of 2,866 RECs for the depth measurements, representing all RECs across 16 DEMs (Figure 3 and Table 1), and 2,725 craters for rim height measurements (a few craters were excluded due to superposition/crosscutting of rims by other landforms). Figure 9 provides *d*/*D* and *h*/*D* plots for the full data set (see supporting information Data Set S1 for all morphometry data). Each crater on the plot was also classified using the morphologic, 1 to 5 classification scheme. As a group, each class follows a general trend that is consistent with inferred states of crater degradation, such that *d* and *h* decrease with each inferred older class. However, notable overlaps exist between each class on the plots suggesting that the morphologic classification scheme is not in perfect agreement with the morphometry and that some morphometric variation occurs between the classes. For Classes 2, 3, 4, and 5 (Class 1 are small and few in number), the linear fits for *d*/*D* are $d = 0.081D$ ($R^2 = 0.99$, $P = 4.63 \times 10^{-223}$), $d = 0.078D$ ($R^2 = 0.97$, $P = 0$), $d = 0.063D$ ($R^2 = 0.88$, $P = 0$), and $d = 0.046D$ ($R^2 = 0.76$, $P = 0$), respectively (Figure 9a and Table 2). These relationships are linear at the 10- to 100-m scale, consistent with *d*/*D* relationships for small lunar craters (R. J. Pike, 1974). They also suggest a shallow depth relative to diameter as compared to the previously published $d \sim 0.02D$ relationship for pristine Martian and lunar craters that are <1 km in size (e.g., Daubar et al., 2014; R. J. Pike, 1974; Watters et al., 2015; Figure 10a). The highest measured *d*/*D* of any crater in the data set, at 0.15, is derived from a 47-m-diameter Class 2 crater (Figure 10a).

Considering the relationship between rim height and diameter, the fit for Class 2 craters is $h = 0.029D$ ($R^2 = 0.96$, $P = 4.65 \times 10^{-154}$), for Class 3 craters it is $h = 0.024D$ ($R^2 = 0.88$, $P = 2.26 \times 10^{-187}$), for Class 4

Table 2
Regression Statistics for the Depth Versus Diameter and Rim Height Versus Diameter Plots Including the Measurements From the Manual Profiling Method (Figures 8a and 8c; Sweeney et al., 2016) and the Complete Results From the Semiautomated Method (Figures 9a and 9c)

Class	R^2	*P* value	Standard error	Standard deviation	*N*	Equation
Depth[a]						
2	0.98	9.08×10^{-35}	1.48	9.25	39	$d = 0.08D$
3	0.95	2.56×10^{-48}	1.61	13.74	73	$d = 0.075D$
4	0.88	1.15×10^{-66}	1.76	21.14	145	$d = 0.053D$
5	0.82	6.1×10^{-97}	1.21	19.49	259	$d = 0.036D$
Rim height[a]						
2	0.96	7.12×10^{-25}	0.75	4.42	35	$h = 0.026D$
3	0.88	1.57×10^{-33}	0.81	6.81	71	$h = 0.024D$
4	0.70	4.65×10^{-12}	0.68	4.39	42	$h = 0.021D$
5	0.87	5.82×10^{-23}	0.54	3.89	51	$h = 0.016D$
Depth[b]						
2	0.99	4.63×10^{-223}	1.25	19.36	239	$d = 0.081D$
3	0.97	0	1.04	22.04	449	$d = 0.078D$
4	0.88	0	1.37	45.04	1,083	$d = 0.063D$
5	0.76	0	1.48	48.66	1,083	$d = 0.046D$
Rim height[b]						
2	0.96	4.65×10^{-154}	0.89	13.26	220	$h = 0.029D$
3	0.88	2.26×10^{-187}	0.71	14.44	409	$h = 0.024D$
4	0.82	0	0.67	21.64	1,044	$h = 0.021D$
5	0.77	0	0.67	21.66	1,048	$h = 0.017D$

[a]Manual data set, Sweeney et al. (2016). [b]Complete semiautomated data set; this study.

craters it is $h = 0.021D$ ($R^2 = 0.82$, P = 0), and for Class 5 craters, $h = 0.017D$ ($R^2 = 0.77$, $P = 0$; Figure 9c). The highest h/D ratio comes from a 37-m-diameter Class 2 crater and is 0.08, although this crater is an outlier (Figure 10b). The Class 2 rim height-diameter relationship is similar to the $0.036D$ relationship for pristine lunar craters of similar size (R. J. Pike, 1977). There is significantly more scatter in the data for the more degraded classes caused by an abundance of rim gaps that provide near-zero rim height minima (Figure 9c). Figure 11 compares depth and rim height values, normalized to crater diameter. The overall distribution of the data between the classes generally supports the observational-based classification scheme, although important scatter is evident. The spread in both depth and rim height values is likely the result of variation in the initial morphometry of each crater (e.g., rim gaps and variations in interior slope) as well as differences in degradation through time. Both will be evaluated in subsequent sections. Because the 1 to 5 classification scheme incorporates multiple morphologic characteristics of the crater exterior and interior (many of which are diameter independent) and because it is reasonably well correlated with the measured crater morphometry, it is used below to establish a time series of degradation.

4. Time Series of Degradation for the RECs

The SFD of RECs within specific morphologic class groupings, Class 1 to 5, 1 to 4, 1 to 3, and 1 to 2, were plotted using CraterStats 2 (Michael & Neukum, 2010) against crater production and chronology functions for Mars (Hartmann & Neukum, 2001; Ivanov, 2001; Michael, 2013; Figure 12). The SFD of craters in each class grouping provides a generalized retention timescale for each class and allows for an evaluation of the rates at which craters degrade from one class to the other. A similar method was employed in Warner et al. (2010, 2017), Golombek, Warner, et al. (2014), and Golombek et al. (2017) to estimate rates of crater degradation using crater morphology. The crater count and age analysis does not account for an increase in crater diameter over the exposure history of the craters (Xie et al., 2017). Cumulative and differential plots were created here for comparison. Model age fits were applied to the distribution of each class grouping where the distribution follows established crater production functions. For example, all Class 1 to 5 craters follow a production slope above 200 m in diameter on the cumulative and differential histograms (Figure 12). This occurs because (1) all Class 1 to 5 craters above this size are RECs and (2) all Class 1 to 5 craters above this size that formed at this location are still preserved; that is, all members of the most degraded REC class (Class 5) are accounted for. A fit to the Class 1 to 5 grouping therefore provides a general crater retention age for all ≥200-m-diameter craters that still exhibit rocks in their ejecta. Fits to younger class groupings (e.g., Class 1 to 4) yield the general timescales over which fresher classes are preserved.

The fit of the data within each class to the production slope at $D \geq 200$ m implies that the classification scheme correlates well with retention age across this range of diameters. In other words, despite the larger volume, a Class 2, 500-m-diameter crater (for example) has the same general retention age as a Class 2, 200-m-diameter crater. This may be in part because several of the morphologic attributes used to classify the relative age of the craters (e.g., superposed craters, indurated infill, and bedforms on floors of craters) are processes that operate independently of crater scale. The fit over this range may also indicate that craters of this size undergo rim and ejecta degradation at relatively similar rates and therefore exhibit a similar and predictable sequence of morphologic change through time (i.e., topographic rounding of the rim and disappearance of meter-size rocks). However, model age fits were not applied below the 200-m-diameter threshold where a roll-off in the SFD of each class is indicated. The roll-off is in part due to the exclusion of smaller, fresh NRECs. The loosely consolidated, granular regolith buffers smaller impactors from hitting the rocky unit at depth. This prevents formation of small RECs in favor of small NRECs (Warner et al., 2017). In addition, the roll-off is a function of the preferential obliteration of smaller craters over the exposure timescales of the

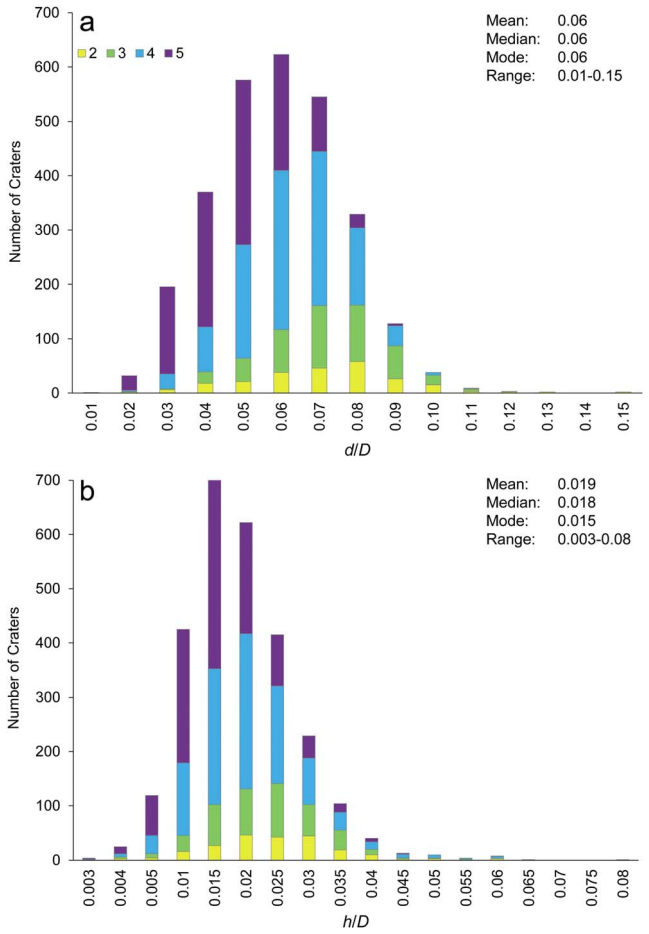

Figure 10. Number of rocky ejecta craters (RECs) per diameter-normalized depth and rim height. Colors relate to the morphometric classification system. (a) Most craters exhibit an intermediate *d/D* relationship, consistent with observations that the majority of RECs are somewhat degraded. The modal *d/D* is 0.06. The maximum *d/D* value is derived from a single Class 2 crater and is 0.15. Pristine *d/D* relationships predict *d/D* ~ 0.2 for fresh craters (e.g., Daubar et al., 2014; Garvin et al., 2003; Pike, 1974; Watters et al., 2015). (b) The modal *h/D*, 0.015, is in agreement with observations that most RECs show evidence of rim modification. The maximum *h/D* value is an outlier at 0.08. Pristine *h/D* relationships predict *h/D* ~ 0.036 for fresh craters (e.g., Garvin et al., 2003; Pike, 1977; Watters et al., 2015).

terrain at the InSight landing site. To demonstrate this, Figure 13 (from Warner et al., 2017) displays three SFDs including (1) all RECs, (2) a subset sample of fresh NRECs plus the RECs, and (3) all craters, regardless of degradation state or rocky ejecta. The NREC plus REC plot represents just a sample of all relatively fresh craters (regardless of rocks in their ejecta) in a portion of the InSight landing site (E9) that have a Class 1 to 5 rim and interior morphology. The reduction in the slope of the distribution on this plot at $D < 200$ m follows the -2 power law function that is typical of an equilibrium population (Hartmann, 2005) and is unrelated to the regolith buffering effect (as small NRECs are now included). This indicates a progressively younger retention age for craters below 200 m in diameter. For example, a 200-m-diameter Class 5 crater has an older crater retention age relative to a 100-m-diameter Class 5 crater, which is older still relative to a 50-m-diameter Class 5 crater.

For the cumulative model age fits at $D \geq 200$ m (Figure 12a), a resurfacing correction was applied to account for the influence of the larger-diameter population (with low sample sizes) following methods in Michael and Neukum (2010). The fit includes 153 RECs with $D \geq 200$, $54 \geq 300$, $14 \geq 400$ m, and only 8 craters with $D \geq 500$ m. The largest diameter crater in the data set is a single 1.2-km crater. The cumulative model ages are 660 ± 50 Ma for all RECs (Class 1 to 5), 430 ± 40 Ma for Class 1 to 4 craters, 340 ± 40 Ma for Class 1 to 3 craters, and 180 ± 30 Ma for Class 1 to 2 craters. Class 1 craters were excluded from fitting due to the limited sample size (12 craters). Errors on the model ages are representative of standard counting error (assuming Poisson sample distribution) and are derived from the square root of *n* (number of craters). For comparison to the derived model ages of the RECs, the maximum age of the entire crater population, including all degraded NRECs (Class 6) that are 200 m to 2 km in diameter is 1.7 ± 0.1 Ga (Warner et al., 2017).

Figure 12b presents the differential plot. There is scatter in the retention ages between each individual diameter bin (10 per decade binning) and between each class. For example, the crater retention age of the 200-m-diameter bin within the Class 1 to 5 grouping is ~430 Ma. The retention age is higher at ~650 Ma for the 251-m bin. For the 316- and 398-m bins, the age varies from ~900 to ~500 Ma, respectively. There is no systematic increase or decrease in the retention age with increasing diameter bin at $D \geq 200$ m that might suggest a relationship between crater retention age and diameter. A differential fit to the $D \geq 200$-m population for each class is therefore used here and provides a general retention age for all class groupings. The model ages are 590 ± 70 Ma for Class 1 to 5, 370 ± 40 Ma for Class 1 to 4, 280 ± 50 Ma for Class 1 to 3, and 130 ± 50 Ma for Class 1 to 2.

In summary, the crater distributions at $D \geq 200$ m on the cumulative and differential plots confirm that degradation between each crater class requires approximately 100 to 200 Myr. The crater retention ages derived from the cumulative method for the entire $D \geq 200$-m population are used below to constrain degradation/erosion rates and as inputs in a slope diffusion model. While specific degradation/erosion rates are given and evaluated for trends (e.g., increase or decrease in rates through time), the order-of-magnitude rates are emphasized here due to the uncertainties in the morphometry measurements and crater chronology (i.e., assumption of a single retention age for each class at $D \geq 200$ m).

5. Crater Degradation and Erosion Rates

Changes in crater depth over time are the result of crater infill, slope modification, and rim height reduction. It is therefore more appropriate to refer to the rates that are derived from depth changes as degradation or

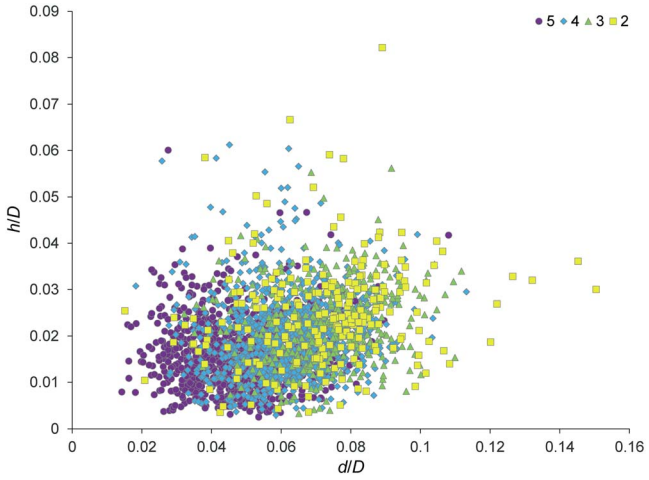

Figure 11. Diameter-normalized depth versus diameter-normalized rim height. Symbols and colors relate to the morphometric classification system. There is a general correlation between crater youth and high values for *d/D* and *h/D*. However, there is significant variability in the data, even among the more pristine Class 2 craters. This suggests that there was significant variability in the morphometric characteristics of these craters in their initial, pristine state or variability in the degradation rates of different craters. The variability in the *h* and *d* characteristics of Class 2 craters in particular argues for some variability in these parameters at formation.

modification rates rather than erosion rates. Changes in rim height can be more closely tied to a true surface erosion rate. At some locations on Mars, rim erosion has been attributed to eolian abrasion, which works to plane off the ejected blocks and reduce the height of the crater rim (Golombek, Crumpler, et al., 2006; Golombek, Warner, et al., 2014; Grant et al., 2006). Diffusive slope processes (e.g., gravity-driven creep) likely play a major role by softening and lowering the interior and exterior regions of the rim by reducing their slopes (Armitage et al., 2011; Fassett & Thomson, 2014; and Golombek, Warner, et al., 2014). Crater rims may also be reduced by subsequent impact events that reworked or gardened the landscape (Hartmann et al., 2001). However, for the younger Amazonian-age RECs, where few craters are observed at HiRISE resolution to superpose the rims, impact gardening was not an important modification process. Rim burial is also possible; however, HiRISE observations suggest that eolian bedforms only partially superpose crater rims (Figures 2, 4c, and 4e). Airfall dust is inefficient at subduing elevated topography; the thermal inertia of the surrounding terrain (~200–250 $J \cdot m^{-2} \cdot K^{-1} \cdot s^{-1/2}$) implies only a thin, optically thick dust coating that is less than 2 mm thick (Golombek et al., 2017).

The maximum retention age from the cumulative SFD of all RECs ≥200 m in diameter is ~660 Ma. Over the approximate length of time of ~480 Myr during which a typical (median in the distribution) 200-m-diameter Class 2 crater degrades to a 200-m-diameter Class 5 crater, *d* decreases from ~21 to ~11 m. This yields a depth-related degradation rate, including crater infill plus rim height reduction, of 0.020 m/Myr (Table 3). Similar order-

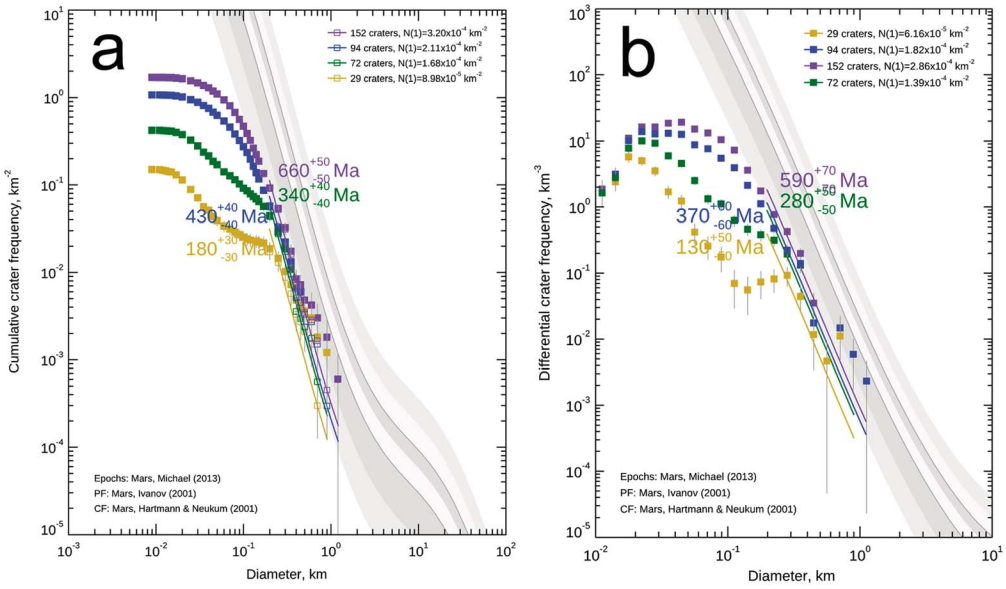

Figure 12. (a) Cumulative crater SFD plots for Class 1 to Class 5 RECs. The cumulative model age fits apply to Class 1–5 craters (purple at 660 Ma), Class 1–4 craters (blue at 430 Ma), Class 1–3 craters (green at 340 Ma), and Class 1–2 craters (yellow at 180 Ma). Gray regions on the plot indicate the epoch boundaries (Michael, 2013). Model age fits to the SFDs were made using a resurfacing correction (Michael & Neukum, 2010) from craters with $D \geq 200$ m. The roll-off in the SFD at $D < 200$ m is attributed to the preferential obliteration of smaller diameter craters and to the presence of a regolith that buffers and prevents the formation of small RECs (see Warner et al., 2017). The second kink in the small crater distribution, notable on the Class 1–2 and Class 1–3 curves at $D < 40$ m, has been attributed to contamination by small secondaries. (b) Differential plot with 10 bins per log decade. A differential model-age fit shows similar relative and absolute age relationships between the classes within each diameter bin. The color code for each class grouping is identical to (a). SFD = size-frequency distribution; REC = rocky ejecta crater.

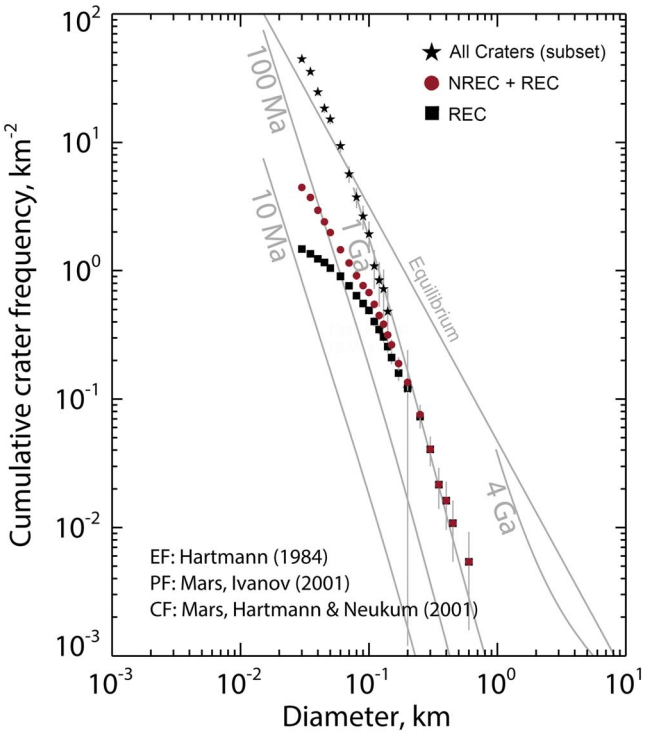

Figure 13. Cumulative size-frequency distribution plot showing the distribution of all RECs, all nonrocky ejecta craters of similar fresh morphology (NREC) + RECs, and all craters regardless of degradation state or rocky ejecta (All Craters). Figure from Warner et al. (2017). The decline in the slope of the distribution at $D < 200$ m for the NREC + REC and All Craters plot suggests preferential obliteration of smaller diameter craters following the Hartmann −2 equilibrium function. REC = rocky ejecta crater; NREC = nonrocky ejecta crater.

of-magnitude degradation rates (~102 m/Myr) occur between individual classes and across different time intervals. Although the calculated standard error ($SD/\sqrt{n}$) for the degradation rates (Table 3) indicates overlap between the values in each grouping, the overall trend in the calculated rates hints at a decrease over increasing time intervals. This trend also persists with inclusion of model age uncertainties (order of ±0.001 m/Myr). Degradation from a Class 2 to a Class 3 crater, over a timescale of 160 Myr, yields a rate of 0.028 m/Myr, compared to the 0.020-Myr^{-1} rate measured over 480 Myr. Rates also decline between individual morphologic classes. From Class 3 to Class 4 the estimated degradation rate is 0.021 m/Myr. From Class 4 to 5 the rate decreases to 0.014 m/Myr. Between Class 5 and Class 6, ~7 m of depth-related change occurs. If we assume a maximum crater age of ~1.7 Ga for the most degraded crater (see Warner et al., 2017), approximately 1 Gyr is required to transition from a rocky Class 5 crater to a Class 6. This yields a significantly lower degradation rate of 0.007 m/Myr and suggests (assuming no change in the surface processes) that the final few meters of depth-related change requires significantly more time than is required for the more dramatic morphologic transitions that occur between the youngest classes.

The depth data also indicate that the degradation rates of larger, 300- to 500-m-diameter craters are similar to the 200 m-sized craters (Table 4). For example, depth reduction for ~400-m-diameter craters over the ~160-Myr time period that separates Class 2 and Class 3 is ~5 m. This results in a similar degradation rate of 0.031 m/Myr. From Class 2 to Class 5, measured over the longer timescale of ~480 Myr, ~400-m-diameter craters degrade by ~12 m. The calculated degradation rate is 0.025 m/Myr. For craters smaller than 200 m, the cumulative crater frequency at specific diameter bins on the NREC + REC plot (Figure 13) was used to estimate crater retention age. For the $D \geq 100$-m-diameter bin, the estimated crater retention age of a Class 5 crater is ~380 Ma (Figure 13). Using the median depth of 4.5 m for a 100-m-diameter Class 5 crater and assuming an initial pristine depth of 15 m (using $d = 0.15D$), the crater degradation rate is 0.028 m/Myr. For $D \geq 50$ m, the maximum crater retention age of a Class 5 is ~130 Ma. Given a median Class 5 depth of ~2.5 m and a pristine depth of ~7.5 m, the

Table 3
Degradation and Erosion Rate Data for the Profile Example at D = 200 m

Class	Depth (*d*; m)	Rim height (*h*; m)	No. of craters (*n*; *D* = 190–210 m)	*d SD* (m)	*d* standard error (m)	*h SD* (m)	*h* standard error (m)
2	20.9	7.0	5	1.5	0.7	1.3	0.6
3	16.4	4.2	11	1.4	0.4	1.6	0.5
4	14.5	3.4	16	2.3	0.6	0.8	0.2
5	11.3	3.0	18	2.5	0.6	1.0	0.2
Class interval	Time interval (Myr)	Degradation rate (m/Myr)	Error (m/Myr)	Erosion rate (m/Myr)	Error (m/Myr)	Start time (Myr)	End time (Myr)
Class 2–3	160	0.028	0.007	0.018	0.007	180	340
Class 2–4	250	0.026	0.005	0.014	0.003	180	430
Class 2–5	480	0.020	0.003	0.008	0.002	180	660
Class 3–4	90	0.021	0.011	0.009	0.008	340	430
Class 4–5	230	0.014	0.005	0.002	0.002	430	660

Note. Standard deviation (*SD*) and standard error ($SD/\sqrt{n}$) are derived from craters within a 190- to 210-m-diameter bin.

Table 4
Summary of Degradation and Erosion Rate Data Comparing Craters of Varying Sizes Measured Over Different Time Intervals

Crater diameter (m)	Time interval (Myr)	Class interval	Degradation rate (m/Myr)	Erosion rate (m/Myr)
400	160	Class 2–3	0.031	0.006
400	480	Class 2–5	0.025	0.004
200	160	Class 2–3	0.028	0.018
200	480	Class 2–5	0.020	0.008
100	380[a]	Class 1–5	0.028	0.006
50	130[a]	Class 1–5	0.039	0.009

[a]Age constraints inferred from crater retention age data (Figure 13) using all available Class 1 to 5 craters within this diameter bin.

degradation rate for 50-m-diameter craters over the 130-Ma time period is 0.039 m/Myr, suggesting an overall faster degradation rate relative to the order of 100-m-diameter population.

By comparison to the depth-related degradation rates, rim erosion rates are typically an order of magnitude lower for all crater sizes (Table 3). For a typical 200-m-sized Class 2 crater, h is ~7 m. For a Class 5 crater, h is ~3 m. Over the ~480 Myr that separates Class 2 from Class 5, the rim erosion rate is 0.008 m/Myr, compared to the 0.020-m/Myr depth reduction rate measured over the same length of time. Similar to the depth reduction rates, rim erosion rates decrease when measured over increased intervals of time and generally decrease between individual classes (Table 3).

For larger-diameter craters, the rim height reduction from a 400-m-diameter Class 2 (h = 11 m) to Class 3 (h = 10 m) crater is approximately 1.0 m. Over ~160 Myr this equates to a rim erosion rate of 0.006 m/Myr (Table 4). From Class 2 to Class 5 (h = ~2.0 m), measured over the period of ~480 Myr, the rim erosion rate is 0.004 m/Myr. At the smaller diameter range, 100-m-sized Class 5 craters have a median rim height of 1.2 m. A pristine rim height is difficult to constrain given the variability in the Class 1 and Class 2 rim height data set. If we assume the $h = 0.036D$ function of R. J. Pike (1977; similar to the $h = 0.029D$ Class 2 function presented here), then the pristine rim height of a 100-m crater is 3.6 m. Over the time period of ~380 Myr that represents the maximum retention age of 100-m-sized Class 5 craters, 2.4 m of rim erosion results in an erosion rate of 0.006 m/Myr, which is similar, given the variability in the rim height measurements, to the rate determined over similar measurement timescales for the 200-m-sized variety. At 50 m, the total rim height reduction between a pristine crater and the Class 5 example is 1.2 m. This results in a rim erosion rate of 0.009 m/Myr, using the maximum age of 130 Ma for Class 5 craters of this size. In summary, all rim erosion rates at all diameter ranges and class groupings are an order of magnitude lower (~10^{-3} m/Myr) than the crater degradation rates (~10^{-2} m/Myr).

6. Diffusion Modeling of Crater Degradation

To quantitatively explore crater degradation, and to interpret the decrease in degradation/erosion rates through time, the transport processes that modify crater topography were modeled as a diffusional process. Armitage et al. (2011), Fassett and Thomson (2014), and Golombek, Warner, et al. (2014) argued that topographic diffusion should be a reasonable approximation of crater degradational processes, where the sediment flux increases with topographic slope. This is likely to be the case for processes such as mass wasting, disturbance-driven creep, and slope-directed eolian transport. Following Golombek, Warner, et al. (2014), the crater profile evolution was modeled using a radially symmetric, nonlinear topographic diffusion model (Pelletier & Cline, 2007):

$$\frac{\partial \eta}{\partial t} = \frac{K}{r}\frac{\partial}{\partial r}\left(\frac{r\frac{\partial \eta}{\partial r}}{1-\left(\frac{|\partial \eta/\partial r|}{S_c}\right)^2}\right) \quad (1)$$

where η is the crater elevation, t is time, r is the radial distance, S_c is the threshold slope for mass wasting by gravity alone, and K is the diffusivity (m^2/year), which characterizes the erodibility of the material and the vigor of erosional and transport processes that modify the crater topography through time.

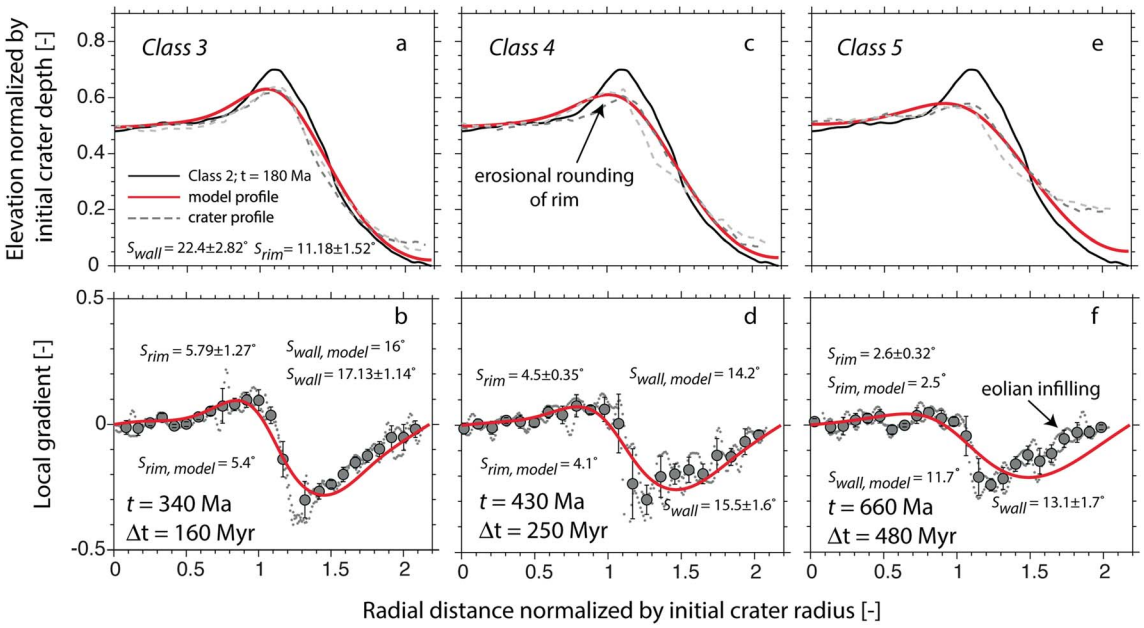

Figure 14. Results of the radially symmetric nonlinear diffusion model (Pelletier & Cline, 2007) with a diffusivity (K) of 8×10^{-7} m^2/year and a threshold slope of 38° (see equation (1)) for craters with diameter 200 m. The initial condition (solid black line in top panels) was chosen to be the averaged half-profile of Class 2 craters. The maximum exterior rim slope (S_{rim}) and interior wall slope (S_{wall}) of the Class 2 crater were 11.18 ± 1.52° and 22.4 ± 2.82°, respectively. The dashed gray lines in the top panels represent the half-profiles of the craters from (a) Class 3, (c) Class 4, and (e) Class 5. The Class 2 profile (age of 180 Ma) was evolved over 160, 250, and 480 Myr to yield the model profiles (solid red lines in top panels) for Classes 3, 4, and 5, respectively. The results are presented in the nondimensional space where the radial distance is normalized by the initial crater radius of 100 m, and the crater elevation is normalized by the initial crater depth (0.15D for Class 2 craters). The bottom panel of figures (b, d, and f) show the local gradients of crater profiles as a function of radial distance normalized by the initial crater radius. The solid red line indicates the model result, the small gray dots are local slope measurements for each of the half-profiles of the crater (gray dashed lines in top panels), and the bigger gray markers are binned averages with associated standard deviation within each bin. Also shown in the bottom panels are the maximum exterior rim slope and maximum interior wall slope for crater profiles of Classes 3, 4, and 5 and their best fit model profiles (labeled here as $S_{rim,\ model}$ and $S_{wall,\ model}$). The observed maximum exterior rim slope and maximum interior wall slope reported here were averaged over a 10-m window and across the two axisymmetric crater half-profiles, that is, the bigger gray markers in the bottom panels. The nonlinear diffusion model adequately represents the erosional rounding of the rim and the crater wall relaxation through time with a near-constant diffusivity.

To avoid dependence of the results on the choice of an initial pristine crater profile, a topographic profile of a typical 200-m-diameter Class 2 crater was chosen as the initial condition for modeling. This crater represents the median example in terms of depth and rim height within the available data set of 200-m craters. Class 1 craters were not modeled as the starting condition because they are small (<50-m diameter), rare in number, and the age constraints are poor. Model runs were also attempted for 400- to 500-m-sized craters, although there is not a significant supply of craters of this size to determine the most typical Class 2 morphology. The Class 2 crater profile at these diameters were reflected around the crater center (axisymmetric) and both sides of the crater profile were averaged to yield a representative initial condition (i.e., half-profile of the whole crater; see solid black line in Figure 14). The time interval between the Class 2 example and older classes determined from the cumulative model age fits ($D \geq 200$ m) were used (Table 3).

For D = 200 m, the radially symmetric nonlinear diffusion model (equation (1)) was numerically solved with the Class 2 crater profile as the initial condition. The threshold slope (S_c) was set to 38° (Golombek, Warner, et al., 2014). The boundary conditions are zero slope at the crater center and zero slope and fixed elevation outside of the crater (i.e., the plains elevation at 1D distance from the rim). The Class 2 crater profile was evolved for 160, 250, and 480 Myr for a variety of diffusivities to yield the model-derived crater profiles for Classes 3, 4, and 5, respectively. The median examples of the measured crater profiles from each of these classes were then reflected around their center and compared with the model results (dashed gray lines in Figure 14). The modeling efforts were focused on reproducing the erosional rounding of the rim through time and in capturing the reduction of the interior crater wall slope. The maximum observed exterior rim slope (S_{rim}) and interior wall slope (S_{wall}) were estimated as the average values computed using central differencing for both the reflected crater half-profiles within each class, which were then averaged over a 10-m

Table 5
Estimated Diffusivities of the Nonlinear Diffusion Model and Model-Derived Erosion Rates With $K = 8 \times 10^{-7}$ m^2/Year

Crater diameter (m)	Estimated diffusivity, K (m^2/year)	
200	7×10^{-7} to 8×10^{-7}	
500	5×10^{-7} to 8×10^{-7}	
200-m-diameter craters	Degradation rate (m/Myr)	Rim erosion rate (m/Myr)
Class 2–3	0.017	0.016
Class 2–4	0.014	0.013
Class 2–5	0.011	0.009

window. For example, the maximum interior wall slope of a crater with D = 200 decreases from 22.4 ± 2.82° (Class 2) to 13.1 ± 1.7° (Class 5). Similarly, the maximum exterior rim slope also decreases from 11.18 ± 1.52° (Class 2) to 2.6 ± 0.32° (Class 5). The best fit diffusivity was determined by finding the model results that minimized the combined percentage error between modeled and observed maximum exterior rim slope ($S_{rim,model}$ and S_{rim}) and maximum interior wall slope ($S_{wall,model}$ and S_{wall}). For each crater class, we explored diffusivities over 4 orders of magnitude from 10^{-4} to 10^{-8} m^2/year at equal increments in logarithmic scale yielding 40 different modeling scenarios. Diffusivities on the order of 10^{-4}, 10^{-5}, and 10^{-8} were readily rejected as these models significantly overpredicted or underpredicted the amount of erosional rounding and crater wall relaxation. The combined percent error between $S_{rim,model}$ and S_{rim}, and $S_{wall,model}$ and S_{wall} for diffusivities within the range of 10^{-6} to 10^{-7} m^2/year was computed.

For D = 200-m craters, the best fit diffusivities that minimized the combined percent error between $S_{rim,model}$ and S_{rim}, and $S_{wall,model}$ and S_{wall} were $K = 7 \times 10^{-7}$ m^2/year, $K = 8 \times 10^{-7}$ m^2/year, and $K = 8 \times 10^{-7}$ m^2/year for Classes 3, 4, and 5 craters, respectively. Further, the models with diffusivities of $K = 7 \times 10^{-7}$ m^2/year and $K = 8 \times 10^{-7}$ m^2/year predicted the observed S_{rim} and S_{wall} within uncertainty (Table 5). Thus, for crater profiles of Classes 3 to 5, the nonlinear diffusion model with a near-constant diffusivity captures the time evolution of the 200-m-diameter Class 2 crater over 480 Myr and describes the erosional rounding of the rim, and the reduction of the crater wall slope with time. Figure 14 shows the results of the numerical modeling for D = 200-m craters with $K = 8 \times 10^{-7}$ m^2/year. The model results are presented in a nondimensional space where the radial distance is normalized by the initial crater radius (in this case, R = 100 m), and the crater elevation is normalized by the initial crater depth ($d = 0.15D$). Further, to compare the shape of the modeled crater profiles and the observed crater profiles for the different classes, the local gradients of the crater profiles were computed and averaged over 10-m window bins and compared with model results (bottom panels of Figure 14). The model-predicted maximum interior crater wall slopes for Classes 3, 4, and 5 craters with D = 200 m were 16°, 14.2°, and 11.7°, respectively, and these predictions match well with the observed maximum interior wall slope of Classes 3, 4, and 5 craters, which were 17.13 ± 1.14°, 15.5 ± 1.6°, and 13.1 ± 1.7°, respectively (Figure 14). In addition, the predicted maximum exterior rim slopes for Classes 3, 4, and 5 craters were 5.4°, 4.1°, and 2.5°, respectively, which match well with the observed maximum exterior rim slopes of 5.79 ± 1.27°, 4.5 ± 0.35°, and 2.6 ± 0.32° for Classes 3, 4, and 5, respectively. However, the model results consistently underpredict the crater floor elevations close to the crater center. For example, the difference between the predicted (with $K = 8 \times 10^{-7}$ m^2/year) and observed elevation of the Class 5 crater at the crater center was 3.9 m, while this value for Class 3 craters was 1.35 m. This is consistent with observations of eolian bedforms on the crater floor that suggest significant infilling. Eolian infilling is not captured by equation (1). If the mismatch of the elevations at the crater center between the model-derived and observed crater profiles is attributed to eolian infilling, then the estimated eolian infilling rate is ~0.008 m/Myr over the averaging timescale of 480 Myr (Class 2 to Class 5 degradation).

Figure 15 shows a comparison between model-derived and the measured rim erosion and crater degradation rates for craters of 200-m diameter (also see Tables 3–5). The rim erosion rate was computed from our model by tracking the decrease in rim height relative to the rim height of the Class 2 crater and normalizing the rim height decrease by the time span over which it was observed. The decrease in rim height over time yielded an estimate of the rim erosion rate over a particular averaging timescale, and this computation was performed for a variety of averaging timescales starting from the initial condition of the Class 2 crater. Depth degradation rates were similarly estimated by tracking the decrease in crater depth relative to the crater depth of the Class 2 crater, that is, the initial condition of the model. Model results indicate that both the rim erosion rates and the depth degradation rates decrease with increase in averaging timescale, consistent with the results obtained from the observed crater morphometry (Table 3). In the model, the average degradation rates and rim erosion rates decrease with time because the crater walls shallow resulting in a decrease in the sediment flux. Thus, the model does not require a change in the surface environment or erosional efficiency (as quantified by a near-constant diffusivity, K) to explain the observed decrease in rim erosion rates in time.

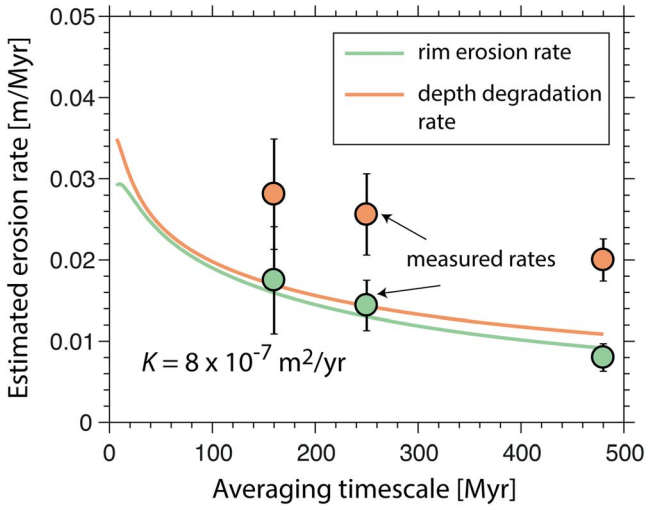

Figure 15. Plot showing the comparison of the model-derived erosion rates with $K = 8 \times 10^{-7}$ m^2/year and the profile-derived erosion rates for craters of diameter 200 m. The model results are shown in solid lines (green corresponds to rim erosion rates, and orange corresponds to depth degradation rates), and the profile-derived erosion rates are shown in markers of the same color as the model prediction. The model-derived erosion rates were computed by using the Class 2 crater as a reference and tracking the decrease in rim height and crater depth with time relative to the Class 2 crater. These estimates were then normalized by the timescale over which the Class 2 crater evolved to yield the estimated rim erosion rate and depth degradation rate. The profile-derived erosion rates correspond to the rates estimated for the Classes 2 to 3, 2 to 4, and 2 to 5 degradation (summarized in Table 3). The error bars on profile-derived rates were estimated by averaging over the decrease in rim heights and crater depths for craters within the size window of 190- to 210-m diameter. The model predictions match the profile-derived rim erosion rates well (green line and markers); however, the profile-derived degradation rates are consistently higher than the model predictions (orange line and markers).

The topographic profiles of craters with diameters between 400 and 500 m were compared with the results of the nonlinear diffusion model using the same chronology derived for craters of size $D \geq 200$ m (see supporting information Figure S4). Similar to the 200-m-diameter craters, the Class 2 crater profile was chosen as the initial condition for the diffusion model for other sized craters. The same threshold critical slope of $S_c = 38°$ was used. The best fit diffusivities for 400- to 500-m-diameter craters ranged from $K = 5 \times 10^{-7}$ to $K = 8 \times 10^{-7}$ m^2/year, which overlapped with the derived diffusivity values for the 200-m-diameter craters of $K = 7 \times 10^{-7}$ to $K = 8 \times 10^{-7}$ m^2/year (Table 5). We did not perform the diffusional modeling on craters of diameter 50 and 100 m because the chronology of each class has not been resolved for the entire InSight landing site. NRECs have yet to be completely mapped across the entire region. However, the roll-off in the crater size-frequency data and the calculated crater retention ages for <200-m-diameter craters suggests that the smaller population degrades faster when compared to ≥200-m-diameter craters (Table 4).

7. Discussion

7.1. Pristine Crater Relationships

The data indicate that even the freshest Class 1 and Class 2 craters at the InSight landing site deviate from the pristine *d*/*D* models suggested for simple lunar and Martian craters (Garvin et al., 2003; R. J. Pike, 1974, 1977; Watters et al., 2015), while rim height and diameter relationships tend to be comparable, but with significant scatter. Morphometric analyses of approximately 150 fresh, 100-m-scale lunar impact craters suggested a depth to diameter ratio of 0.20 (R. J. Pike, 1974) and rim height to diameter ratio of 0.036 (R. J. Pike, 1977). From a global evaluation of fresh, kilometer-sized Martian impact craters in Mars Orbiter Laser Altimeter data, Garvin et al. (2003) found that simple craters follow the relationships $d = 0.196D^{0.96}$ and $h = 0.03D^{0.96}$ (d, D, and h measured in kilometers). Watters et al. (2015) examined 384 small Martian craters across the globe with diameters ranging from 25 m to 5 km in HiRISE DEMs, fitting similar power law functions of $d = 0.205D^{1.012}$ (d and D measured in meters) and $h = 0.0354D^{1.017}$ (h and D measured in meters). Finally, Daubar et al. (2014) reported a $0.23D$ relationship with depth for recently formed decameter-scale Martian craters. By comparison, the crater with the largest *d*/*D* ratio in the InSight landing site is a 47-m Class 2 crater with a ratio of 0.15. Class 1 craters, which are mostly <50 m in diameter, are shallower than this Class 2 example. A linear fit to the entire Class 2 data set suggests a *d*/*D* ratio of 0.08. The causes for the generally lower *d*/*D* ratios for the freshest available craters in the study area are explored below and could be due to (1) target properties and/or (2) relatively rapid eolian infill.

7.1.1. Target Properties

The lower *d*/*D* may be a result of the presence of a regolith at the InSight landing site. The strength and stratigraphy of the target terrain strongly influences crater morphology, causing craters that are observationally pristine, based on some characteristics, to have low *d*/*D* values (e.g., Gault et al., 1968; Mizutani et al., 1983; Moore, 1971; Robbins & Hynek, 2012). R. J. Pike (1980) and Stewart and Valiant (2006) found shallow pristine Martian craters on surfaces composed of weak, volatile-rich materials. The equatorial location of western Elysium Planitia, however, lacks periglacial or glacial landforms (Golombek et al., 2017) that might indicate volatiles at depth. Impacts into a two-layer stratigraphy composed of bedrock overlain by loosely consolidated regolith also generate shallow, flat-floored and nested craters (Bart, 2014; Bart et al., 2011; Oberbeck & Quaide, 1967; Quaide & Oberbeck, 1968; Senft & Stewart, 2007; Wilcox et al., 2005). Stopar et al. (2017) report a range of *d*/*D* ratios from 0.11 to 0.17 for a set of 930 simple lunar craters from 40 m to 10 km in diameter that is more consistent with the InSight region. They suggest that the dominance of relatively shallow, 10- to 100-m-scale craters on a variety of lunar terrains is the result of a poorly cohesive regolith. Watters et al.

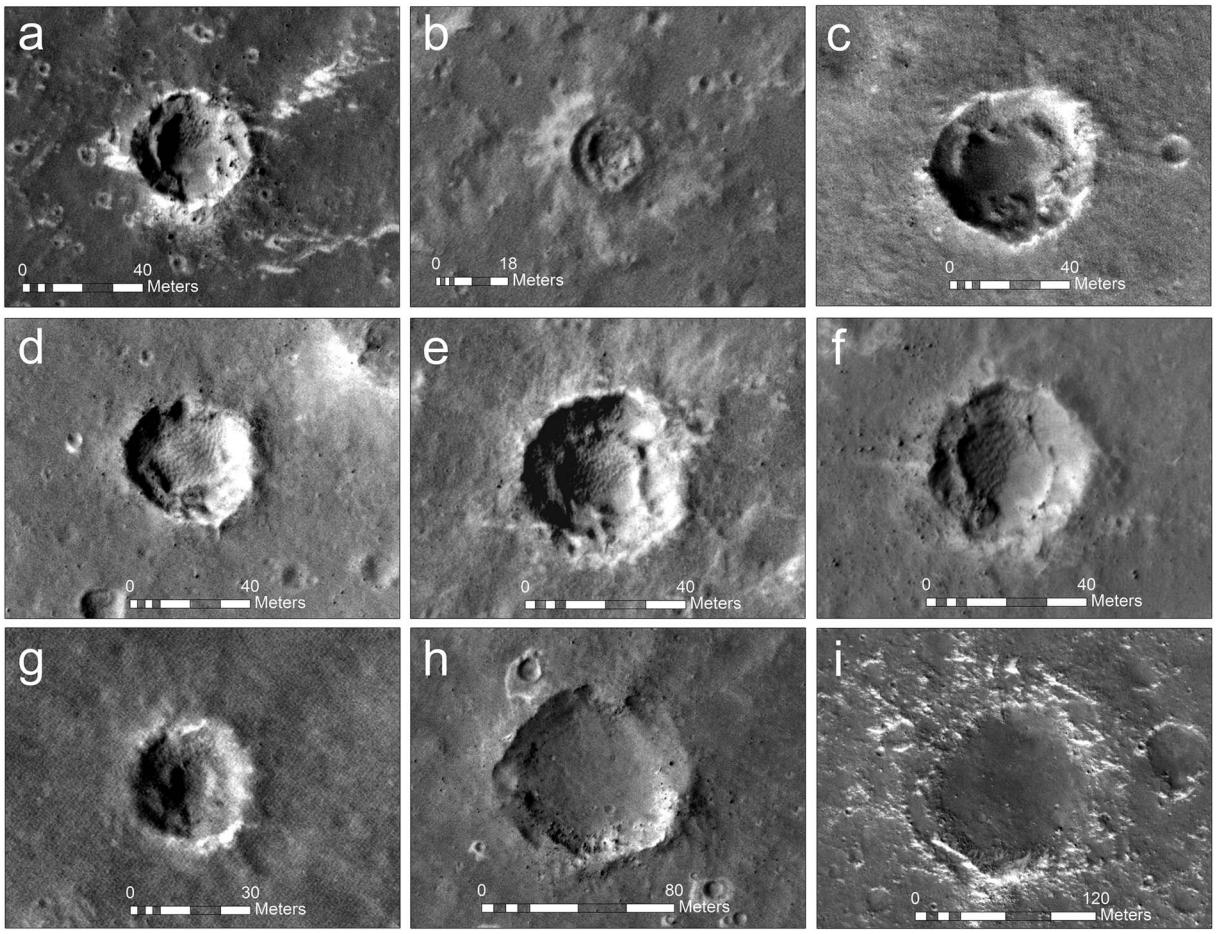

Figure 16. Examples of nested (or concentric) craters in the InSight landing region from Warner et al. (2017). Images (a)–(g) represent fresh Class 1 and Class 2 nested craters. Image (h) is a degraded Class 4 nested crater, and image (i) is too degraded to be classified as a rocky ejecta crater, but the inner ring indicates the presence of a competent rocky unit.

(2015) also report lower *d/D* ratios of 0.15–0.18 for Martian craters in cohesionless or poorly consolidated material. Shallow, flat-floored morphology results from an impact that is able to excavate the regolith but not the more competent bedrock beneath it. For nested craters, a wider crater is initially excavated within the relatively loose regolith. However, a component of the impacting energy is required to first fracture the underlying bedrock before that material can be exhumed, resulting in a smaller crater that marks the contact with the more resistant unit. Nested craters are common across the InSight landing site and dominate within the diameter range of 20 to 100 m (Figure 16). The lower *d/D* values presented here therefore support the previous observations of a loosely consolidated, rock-free surficial regolith at this location (Warner et al., 2017).

7.1.2. Crater Infilling and Rim Modification

While the diffusion model is capable of capturing the overall pattern of rim height reduction through time, the models do not match the measured depths and interior slope profiles near the center of the craters. The disparity between the diffusion model and measured changes in depth, along with the observations of eolian bedforms within the craters, suggests that eolian infill plays an important role in the degradation sequence and may be another key factor that explains the relatively low *d/D* of even relatively pristine craters (see Figures 10 and 14). By comparing the diffusion model results to measured crater profiles, the rate of eolian infill is estimated at ~0.008 m/Myr, measured over the time interval that spans Class 2 to Class 5 (480 Myr). Infill therefore accounts for approximately 30% to 40% of the total depth-related degradation over that time period. The remainder is related to slope relaxation through diffusional processes. However, it is unclear whether the eolian infill rate is constant through time. Observations of sub-meter

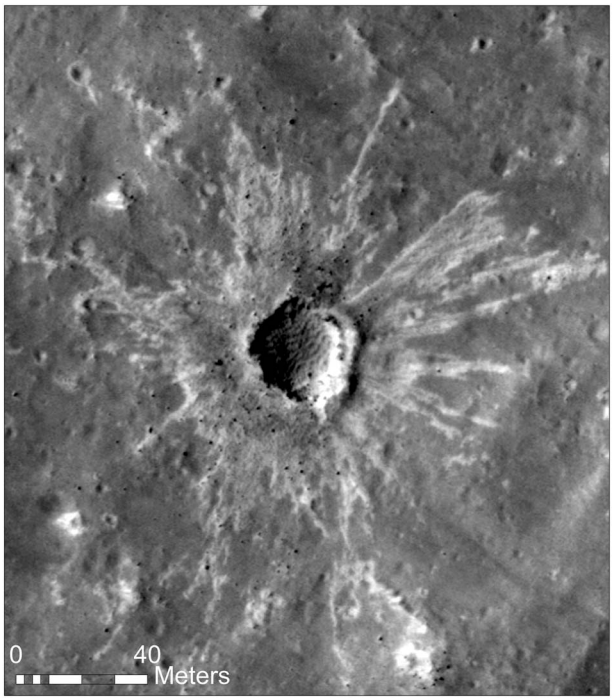

Figure 17. Secondary crater from the 1- to 2.5-Ma Corinto crater. Corinto secondary craters are recognized by the bright lobate ejecta around the crater. This ~30-m-diameter crater also has rocks in the ejecta and bedforms have accumulated on the crater floor. A nested crater morphology is also observed. Image ESP_35640_1845.

to meter-scale eolian bedforms on the floors of Class 1 and 2 craters (Figures 2, 4a, and 5), including secondary craters derived from the 1- to 2.5-Ma Corinto crater (Hundal et al., 2017; Figure 17), suggest that a mobile sand supply is deposited at the earliest stages of crater modification, thus explaining some component of the low *d/D* ratios for pristine craters. However, if the Class 2 to 5 time-averaged crater infill rate is used to calculate infill over the period since formation of the Corinto secondaries, then these craters should exhibit negligible fill. Furthermore, over the maximum timescale that separates a pristine crater and a Class 2 crater (~180 Myr), the Class 2 to 5 eolian infill rate would only account for ~1.4 m of crater fill, which is less than is suggested given the wavelengths of the observed meter-scale bedforms that are found within these craters (Figures 2 and 4). This implies that either the early infill rate is higher relative to the time-averaged rate or that the interior bedforms observed in the relatively young craters are temporary. The latter explanation is unlikely given the observations of increasing sedimentary infill with increasing crater degradation state across the entire region and at all crater diameters. There are no examples of a degraded crater that lacks trapped sedimentary infill.

The crater morphometry data further suggest that the rate of depth-related degradation decreases by approximately a factor of 2 through time, ranging from 0.028 m/Myr between Classes 2 and 3 to 0.014 m/Myr between Classes 4 to 5. This may be partially reflective of an overall reduction in rim erosion rates, which change from 0.007 m/Myr for Classes 2 to 3 to 0.002 m/Myr for Classes 4 to 5. As the crater ages, height reduction of the rim and lowering of the interior slopes reduce the rates of modification by diffusion because the sediment flux increases nonlinearly with the local topographic slope. While the rate of rim erosion by eolian abrasion may decrease as the rim becomes less of a topographic obstacle to wind-blown sand, the diffusion model suggests that slope relaxation alone can explain the entirety of the observed rim height change. However, the reduction in depth-related degradation rates may also be related to a reduction in eolian infill rates (Tables 3 and 4). An impact crater becomes less of a topographic sink for wind-blown sediment as the crater fills, thus decreasing the rate of infill with time. If there is a limited sand supply, the infill rate will also decrease as the supply becomes exhausted. HiRISE images demonstrate that bedforms are scarce in the intercrater regions of the landing site but are common in the ejecta blankets of Class 1 and 2 craters. This suggests that the sand supply that is involved with filling impact craters here is derived from the impact process and is mobilized directly from the ejecta (Figure 2). Fragmentation theory developed by Charalambous (2015) shows that repeated fracture events result in a particle size distribution described by a negative binomial. Application to the InSight landing site based on rock abundances from orbit and surface counts from the *Spirit* and *Phoenix* landers (Golombek et al., 2017) can be extrapolated to sand size particles and show that enough sand can be produced via fragmentation from the observed cratering since the basalt was deposited to comprise most of the observed regolith (Charalambous et al., 2017). This suggests that the sand is dominantly impact produced in agreement with McGlynn et al. (2011) and W.T. Pike et al. (2011). Immediately after impact and fragmentation of the regolith and rockier strata, the fine-grained component of the ejecta is out of equilibrium with the local aerodynamic regime. Short-term sediment transport rates are therefore expected to be relatively high, consistent with the partial infilling of the youngest craters at the InSight landing site and at other landing sites (e.g., Golombek, Crumpler, et al., 2006; Golombek, Grant, et al., 2006; Grant et al., 2004, 2006). Golombek, Warner, et al. (2014) found that the rate of modification at Meridiani Planum, for example, soon after impact, can be as high as 1–10 m/Myr but then decreases with time as the crater degrades. The impact-generated sand fills hollows and craters in the terrain, ultimately resulting in a smooth soil surface (e.g., Smooth Terrain). This sequence is observed at the InSight landing site in the degradation of the crater interiors from Class 1, where bedforms are evident, to Class 4, where the fill becomes completely smoothed off.

7.2. Size Dependent Crater Degradation at the InSight Landing Site

The morphometric and chronologic data suggest important differences in the rate of crater modification/obliteration between 10 and 100-m-scale craters at the InSight landing site. The SFD of all relatively fresh (RECs + NRECs) <200-m-sized craters indicate that 50- and 100-m-sized Class 5 craters are retained over shorter timescales when compared to ≥200-m-diameter Class 5 craters. The maximum retention age for 50-, 100-, and 200-m-sized Class 5 craters is ~130, ~380, and ~660 Ma, respectively. The analysis here demonstrates that while crater rim and slope modification can largely be modeled by diffusion, depth-related changes also require an influx of eolian sediment to the interior of the crater. The question is whether this influx alone can explain the faster rates of crater obliteration for smaller craters or if diffusional processes are also sensitive to crater size. Using the time-averaged eolian infill rate of 0.008 m/Myr, calculated from a comparison of the Class 2 and Class 5 diffusion profiles, a pristine 50-m-diameter crater with a depth of 7.5 m ($d = 0.15D$) requires ~940 Myr to completely fill. Modification of a pristine crater to become a typical 50-m-diameter Class 5 crater with a depth of 2.5 m results in ~5 m of depth change. This would require 620 Myr at the given fill rate. A factor of 2 longer timescale, or 1.9 Gyr, is required to completely fill a 100-m-diameter crater with eolian material and ~1.3 Gyr is required for a 100-m-diameter crater to change from a pristine state to Class 5. Finally, for 200-m-diameter craters, 3.8 Gyr is needed to completely fill the crater and 2.4 Gyr is required to modify a pristine crater to the Class 5 state. Time estimates for the modification and complete obliteration of 50- to 200-m-sized craters at the landing site by eolian infilling far exceed the maximum retention age of the craters, confirming that eolian infill alone cannot account for all of their depth-related degradation.

A likely possibility for the lower retention age of the smaller-sized craters may relate to the rate of diffusional modification and delivery of sediment from the interior crater slopes. Within the diffusional framework, the sediment flux on the interior walls of the craters is directly proportional to the slope of the walls, that is, for a given diffusivity, the sediment flux is higher on steep slopes compared to shallow slopes. To evaluate slope differences, multiple 50-, 100-, and 200-m-diameter Class 2 RECs were measured using the HiRISE DEMs. The maximum interior crater wall slope of a 50-m-diameter REC (sample size of 10 craters), which is assumed to have impacted into a more competent rocky unit, is 19.2° ± 3.6° (averaged over a 10-m length scale). A similarly fresh, nonrocky, 50-m-diameter crater that is assumed to have impacted into a granular regolith, has an average wall slope of 11.6° ± 3.6° (sample size of seven craters). The lower slope of the nonrocky variety is likely related to the weaker mechanical properties of the regolith. By comparison, the maximum interior wall slopes averaged over a 10-m length scale for 100- and 200-m RECs are 18.4° ± 3.7° (sample size of five craters) and 22.7° ± 4.1° (sample size of seven craters), respectively, which are similar to the interior slopes of 50-m RECs. There are no nonrocky varieties at this larger-diameter range. While the 50-m-diameter craters that impacted into granular regolith have lower slopes compared to the craters of similar size that impacted into rockier material, the diffusional modification of craters that impacted into the regolith is likely faster because the walls are composed of unconsolidated material, which are mobilized more readily by diffusional processes. However, for the craters that impacted almost entirely into more competent rock, the maximum interior crater wall slope does not vary substantially with crater diameter. Therefore, the rate of slope modification does not vary substantially for the RECs. The diffusional modeling exercise also derived a similar diffusivity for 200- to 500-m-diameter craters using the same degradational timescales, which suggests that the efficiency of slope modification for RECs is similar across a broad range of crater diameters. The observed increase in the rate of modification and obliteration for <200-m-sized craters is therefore only a function of the low volume of their interior cavity and susceptibility to more rapid infill over the exposure timescales, particularly for the nonrocky variety which fill more rapidly by slope modification.

7.3. Complexity in Crater Modification Through Time

The morphometric data suggest that changes to rim height and depth over time are not as well correlated as the morphologic observations and diffusion models might suggest (Figure 11). For example, diffusional slope processes should consistently fill craters as their rims are reduced in height. Wind-blown sand and dust accumulation should also provide a consistent time sequence of fill for all craters in the landing site. However, there is important variability in the morphometry (d and h) of 100-m-scale craters that indicates complexity and potentially, variation in the relative dominance of certain processes that influence crater form and

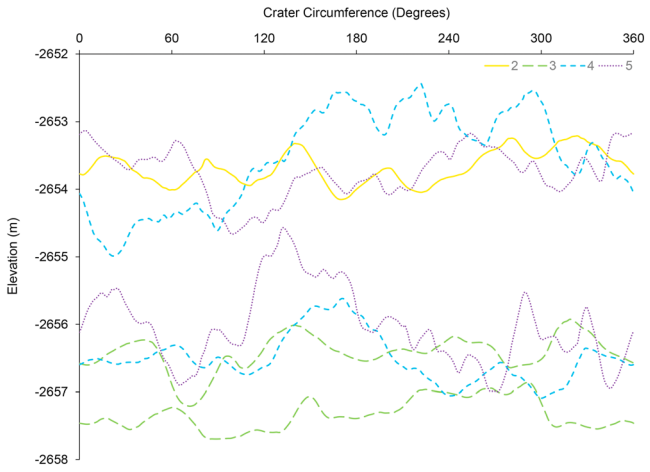

Figure 18. Variable rim crest elevation around the circumference of seven rocky ejecta craters with D = 200 m, coded by class. North is at 0°. Crater rims are topographically irregular at all classes but particularly with the passage of time as large gaps or notches develop. Colors and symbols (e.g., dashes and dots) relate to the morphometric classification system. The total difference in rim elevation for each profile is (from top to bottom along the y axis): 1.54 m (Class 5), 0.94 m (Class 2), 2.54 m (Class 4), 2.42 m (Class 5), 1.28 m (Class 3), 1.47 m (Class 4), and 0.83 m (Class 3).

modification history (e.g., impact dynamics, target stratigraphy, availability of sand supply, and atmospheric conditions).

A similar scatter in the correlation between rim height and depth was identified from 100-m-scale to 1 km-scale Martian craters by Watters et al. (2015). In that study, while a reduction in d/D was statistically correlated with observed crater modification through time, a significant correlation was not identified between h/D and time. The RECs at the InSight landing site do show a good correlation between both d/D and h/D and the relative age of craters (Class 1 to 5; Figure 9). However, the lower R^2 values for the linear fits to each class on the h/D plot suggest that rim height does not correlate as strongly with class and time as does depth. This is likely due to the large variability that exists between the measured rim heights of different craters within a single class, especially for the larger Class 2 craters. There is also large variability in the rim height and interior slope for a single crater. Many craters exhibit notches or gaps in their rims, suggesting nonuniform rim formation or nonuniform rim reduction (Figure 18), where rims degraded faster at specific locations around their circumference.

Because degradation is sensitive to the initial and intermediate morphologic state of a crater, this morphologic variability would result in a less predictable modification sequence. For example, while eolian abrasion may only play a minor role in the overall, uniform reduction of crater rims, the notches or gaps may represent regions of enhanced localized abrasion, or wind gaps. Bedforms, and thus the abrading sand supply, more commonly organize along the NW outer edge of craters in the InSight landing site, and to a lesser extent the SE outer edge (Figures 2, 4, and 19). This is consistent with the regional winds (Reiss & Lorenz, 2016) that may have supplied and organized sand at these locations. It is also consistent with the trend of dust devil tracks observed in HiRISE images (Figure 19).

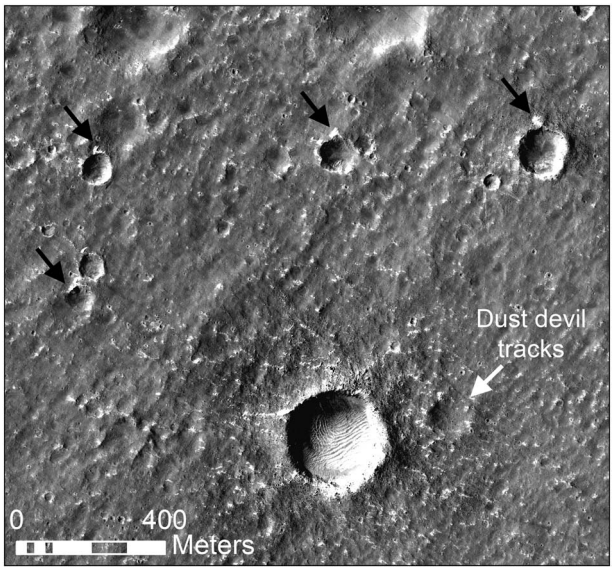

Figure 19. Preferential bedform accumulation (black arrows) along the northwest quadrant of multiple crater rims in the Interior Exploration using Seismic Investigations, Geodesy and Heat Transport landing region. The faint dark streaks oriented NW-SE near the largest crater (Class 2) are dust devil tracks. High-Resolution Imaging Science Experiment image ESP_035640_1845.

The diffusion modeling suggests that the observed rim modification may be the sole result of slope processes. Therefore, a possible explanation for the spread in the morphometric data is the variability in the target stratigraphy and therefore erosional competence of the substrate (e.g., presence or absence of a regolith or competent layer). Warner et al. (2017) suggested the possibility for horizontal and vertical variations in the stratigraphic architecture of the upper ~18 m of the substrate across the InSight landing site that would strongly influence the starting morphometry and resulting degradation of 10- to 100-m-scale craters. The inferred stratigraphy consists of a surficial unit comprised of loosely consolidated granular materials that lack meter-sized rocks. This overlies a rockier regolith unit that grades with depth (either gradually or abruptly) into bedrock. The minimum thickness of the rock-free surficial unit is ~2 m, based on the observation of nested/concentric craters and the observation that some 30-m-diameter craters exhibit a few meter-sized rocks in their ejecta (using excavation relationships by Melosh, 1989). Most craters below 30 m in diameter in the landing site completely lack ejected rocks. The maximum thickness of the rock-free surficial regolith unit is 5 m, based on the observation that at other locations in the landing site, larger 50- to 60-m-diameter craters completely lack rocks. The spatial scale of these lateral stratigraphic variations is unknown; however, Warner et al. (2017) identified a region with abundant, small (~30 m) rocky craters that follows the strike of a north-south trending wrinkle ridge, suggesting a locally thin regolith. Ten to 20 km from this ridge, craters of similar size lack rocks.

Above diameters of 50 m, but below 200 m, many but not all fresh craters throughout the landing site exhibit rocks, indicating that there is also vertical variability in regolith thickness, maximum clast size, and sorting characteristics. Furthermore, the rock distribution in the ejecta of the RECs at this diameter range is often discontinuous and the rock abundance is variable (Warner et al., 2017). Above 200 m in size, however, all fresh craters have a continuous rocky ejecta blanket. The variability in the abundance and coverage of rocks in the ejecta for 50- to 200-m-sized craters implies that the rockier unit below the rock-free surficial layer may not be solid, competent bedrock. Rather, craters of this size may have accessed a coarser portion of the regolith column that contains some unknown abundance of meter-sized rocks. Stratigraphic observations from fractures at nearby Hephaestus Fossae, which crosscut Late Hesperian to Early Amazonian terrains, confirms that a granular, surficial regolith lies immediately above a rockier unit that is likely a coarser, basal unit of the entire regolith column (Golombek et al., 2017; Warner et al., 2017). This unit contains loose, 1-m-scale blocks down to depths of 10 to 20 m below the surface. Beneath this, a solid, continuous bedrock layer is observed. The described vertical and horizontal variations in target stratigraphy across the InSight landing site are likely major factors that contributed to variability in both pristine crater morphometry and degradation history.

7.4. Erosion Rates Within the Context of Martian Climate

The rim erosion rates calculated for the InSight landing site are consistently on the order of 10^{-3} m/Myr, measured over timescales of (order of) 100 Myr. More specifically, the calculated erosion rates vary from 0.002 to 0.018 m/Myr over timescales of 90 to 480 Myr. Erosion rates can vary with the time span over which they are measured (sometimes referred to as timescale bias; Ganti et al., 2016; Gardner et al., 1987; Kirchner et al., 2001; Sadler, 1981, 1999; Sadler & Jerolmack, 2014). For example, measured erosion rates can show an apparent increase with decrease in averaging timescale owing to the intermittency in erosion and the incorporation of larger erosional hiatuses with increasing windows of averaging timescale (Ganti et al., 2016). Because of this, InSight rim erosion rates are compared here to those estimated over similar timescales on Mars. Hesperian to Amazonian erosion rates, averaged over 80–400 Myr (compiled in Golombek, Warner, et al., 2014), are derived from (1) the concentration of blueberries at the surface and the degradation of small craters at Meridiani Planum over the Late Amazonian (Golombek, Grant, et al., 2006), (2) erosion of large (diameter $>$ 8 km) Hesperian craters (Warner et al., 2010), and (3) from cosmic ray exposure ages at Gale crater (Farley et al., 2014). These rates vary from 10^{-3} to 10^{-2} m/Myr. All Hesperian to Amazonian erosion rates, measured over time spans of order 100 Myr to 3 Gyr, are generally $<10^{-2}$ m/Myr (see summary in Golombek, Warner, et al., 2014) and thus fall within the same range as the InSight rates. This argues that the InSight region has not experienced a significantly unique set of surface processes as compared to other Hesperian to Amazonian-age surfaces at other landing sites and that crater degradation occurred within a cold, hyperarid climate. Hesperian and Amazonian erosion rates are typically 2 to 3 orders of magnitude slower than Middle and Late Noachian erosion rates (Carr, 1992; Craddock & Maxwell, 1993; Craddock et al., 1997; Hartmann et al., 1999; Hynek & Phillips, 2001; Warner et al., 2010) measured over timescales of (order of) 100 Myr (Golombek, Warner, et al., 2014). The Noachian rates are similar to typical slow continental erosion rates on Earth that are dominated by liquid water (Ganti et al., 2016; Judson & Ritter, 1964; Portenga & Bierman, 2011; Saunders & Young, 1983).

In addition, the diffusion modeling suggests that the measured decrease in erosion rates between different crater classes (Class 2 to 3, Class 3 to 4, etc.) are an expected consequence of the relaxation of topographic slope of craters during their degradation process (Figure 14). The decrease in rates does not require a change in climate or erosional efficiency over the averaging timescales under consideration here, which is exemplified by the constant value of the derived diffusivity (~10^{-7} m^2/year; Figure 14 and Table 5). The diffusivity, which characterizes the erodibility of the material and the vigor of erosional and transport processes, is similar to that determined from the degradation of small Meridiani Planum craters (~10^{-6} m^2/year; Golombek, Warner, et al., 2014). It is also similar to the diffusivity determined for the dry, airless Moon (5.5×10^{-6} m^2/year; Fassett & Thomson, 2014). Diffusivities of ~10^{-6} to 10^{-7} m^2/year that are representative of Mars and the Moon are 2 to 3 orders of magnitude lower than diffusivities on Earth (slow continuous mass movements from Martin & Church, 1997; Saunders & Young, 1983) that are dominated by liquid water and thus are in agreement with slow, dry erosional processes.

8. Conclusion

Semiautomated methods for evaluating the morphometry of RECs at the InSight landing site in western Elysium Planitia capture the key morphometric parameters (depth, diameter, and rim height) of impact craters. The resultant data from these methods demonstrate a general correlation between a reduction in rim heights and depths with observed morphologic changes through time. Crater degradation, defined as depth reduction through time, occurs at a rate that is on the order of ~10^{-2} m/Myr, measured over 90- to 480-Myr timescales. Surface erosion rates, determined by the reduction in rim height through time, are on the order of ~10^{-3} m/Myr. In all cases, degradation and erosion rates decrease with each subsequent degradational class and with an increase in the averaging timescale. The observed time evolution of crater rims and the derived rates are consistent with a nonlinear diffusion model for the topographic evolution of crater profiles and low diffusivity (~10^{-7} m^2/year) consistent with dry mass wasting. Observed depth-related changes, however, are not adequately modeled by diffusion, confirming the importance of eolian infill. The calculated rates indicate that the bulk of crater modification occurs relatively soon after impact. Sand ejected by the impact quickly accumulates against crater rims and deposits within the craters within a few hundred million years of crater formation. Over timescales of ~180 Myr (Class 2 craters), the interiors of impact craters see the development of meter-scale bedforms. Over ~660 Myr (Class 5 craters), craters become almost completely filled. This relatively rapid infilling may in part be responsible for the low *d/D* relationship (0.15) among the most pristine craters, although target properties relating to the presence of a poorly consolidated regolith overlying resistant bedrock also likely play a role. Overall, the crater degradational sequence, defined by Class 1 to Class 5 RECs, suggests dry erosional processes of mass wasting and eolian modification over the past ~1 Ga of Mars history, consistent with other Amazonian to Hesperian-age surfaces on Mars.

Acknowledgments

Research described in this paper was partially done by the InSight Project, Jet Propulsion Laboratory, California Institute of Technology, under contract with the National Aeronautics and Space Administration. Sweeney and Warner were also partially funded through NASA grant NNX14AL09G. Ganti acknowledges support from the Imperial College Junior Research Fellowship. We would like to thank Fred Calef at JPL for his advice with specific GIS methods. We thank JPL interns Claire Schwartz, Deborah Hernandez, Katherine Smyth, Soumya Kannan, and Jeff Green with their help mapping craters. We also thank SUNY Geneseo student Anthony Pivarunas for his help. We are especially grateful to the Mars Reconnaissance Orbiter HiRISE (University of Arizona) and CTX (Malin Space Science Systems) imaging teams for their high quality data and hard work in acquiring InSight imagery. This is InSight contribution 48. HiRISE, CTX, and THEMIS data are available through the NASA Planetary Data System (https://pds.nasa.gov/). HiRISE images and DEMs can also be accessed through the University of Arizona at https://hirise.lpl.arizona.edu/. CTX images were obtained from the Arizona State Universities' CTX Image Explorer at https://viewer.mars.asu.edu/viewer/ctx. All crater morphometry data relevant to the results of this study including measurements of diameter, depth, and rim height are available in supporting information Data Set S1. This includes measurements from the original Sweeney et al. (2016) work.

References

Armitage, J. J., Warner, N. H., Goddard, K., & Gupta, S. (2011). Timescales of alluvial fan development by precipitation on Mars. *Geophysical Research Letters*, *38*, L17203. https://doi.org/10.1029/2011GL048907

Banerdt, W. B., Smrekar, S., Hoffman, T., Spath, S., Lognonné, P., Spohn, T., et al. (2017). The InSight mission for 2018 (expanded abstract), *48th Lunar Planet. Sci. Conf.*, Abstract 1896.

Bart, G. D. (2014). The quantitative relationship between small impact crater morphology and regolith depth. *Icarus*, *235*, 130–135. https://doi.org/10.1016/j.icarus.2014.03.020

Bart, G. D., Nickerson, R. D., Lawder, M. T., & Melosh, H. J. (2011). Global survey of lunar regolith depths from LROC images. *Icarus*, *215*(2), 485–490. https://doi.org/10.1016/j.icarus.2011.07.017

Basilevsky, A. T., Kreslavsky, M. A., Karachevtseva, I. P., & Gusakova, E. N. (2014). Morphometry of small impact craters in the Lunokhod-1 and Lunokhod-2 study areas. *Planetary and Space Science*, *92*, 77–87. https://doi.org/10.1016/j.pss.2013.12.016

Boyce, J. M., & Garbeil, H. (2007). Geometric relationships of pristine Martian complex impact craters, and their implications to Mars geologic history. *Geophysical Research Letters*, *34*, L16201. https://doi.org/10.1029/2007GL029731

Boyce, J. M., Mouginis-Mark, P. J., & Garbeil, H. (2005). Ancient oceans in the northern lowlands of Mars: Evidence from impact crater depth/diameter relationships. *Journal of Geophysical Research*, *110*, E03008. https://doi.org/10.1029/2004JE002328

Boyce, J. M., Mouginis-Mark, P. J., Garbeil, H., & Soderblom, L. A. (2005). History of major degradational events in the highlands of Mars: Preliminary results from crater depth and diameter measurements, *36th Lunar Planet. Sci. Conf.*, Abstract 1050.

Carr, M. H. (1992). Post-Noachian erosion rates: Implications for Mars climate change. *Proceedings of the Lunar and Planetary Science Conference*, *23*, 205–206.

Carr, M. H. (2006). *The surface of Mars*. Cambridge: Cambridge University Press.

Carr, M. H., & Head, J. W. (2010). Geologic history of Mars. *Earth and Planetary Science Letters*, *294*(3–4), 185–203. https://doi.org/10.1016/j.epsl.2009.06.042

Charalambous, C. (2015). On the evolution of particle fragmentation with applications to planetary surfaces, (PhD thesis) Imperial College London.

Charalambous, C., Pike, W. T., & Golombek, M. P. (2017). Estimating the grain size distribution of Mars based on fragmentation theory and observations, Abstract P41C-2843 presented at 2017 Fall Meeting, AGU, New Orleans, LA, 11–15 Dec.

Craddock, R. A., & Howard, A. D. (2000). Degraded Noachian craters: Fluvial versus lava infilling, *31st Lunar Planet. Sci. Conf.*, Abstract 1542.

Craddock, R. A., & Howard, A. D. (2002). The case for rainfall on a warm, wet early Mars. *Journal of Geophysical Research*, *107*(E11), 5111. https://doi.org/10.1029/2001JE001505

Craddock, R. A., & Maxwell, T. A. (1993). Geomorphic evolution of the Martian highlands through ancient fluvial processes. *Journal of Geophysical Research*, *98*, 3453–3468. https://doi.org/10.1029/92JE02508

Craddock, R. A., Maxwell, T. A., & Howard, A. D. (1997). Crater morphology and modification in the Sinus Sabaeus and Margaritifer Sinus regions of Mars. *Journal of Geophysical Research*, *102*, 13,321–13,340. https://doi.org/10.1029/97JE01084

Daubar, I. J., Atwood-Stone, C., Byrne, S., McEwen, A. S., & Russell, P. S. (2014). The morphology of small fresh craters on Mars and the Moon. *Journal of Geophysical Research: Planets*, *119*, 2620–2639. https://doi.org/10.1002/2014JE004671

Daubar, I. J., McEwen, A. S., Byrne, S., Kennedy, M. R., & Ivanov, B. A. (2013). The current Martian cratering rate. *Icarus*, *225*(1), 506–516. https://doi.org/10.1016/j.icarus.2013.04.009

Farley, K. A., Malespin, C., Mahaffy, P., Grotzinger, J. P., Vasconcelos, P. M., Milliken, R. E., et al. (2014). In situ radiometric and exposure age dating of the Martian surface. *Science*, *343*(6169). https://doi.org/10.1126/science.1247166

Fassett, C. I., & Head, J. W. (2008). The timing of Martian valley network activity: Constraints from buffered crater counting. *Icarus*, *195*(1), 61–89. https://doi.org/10.1016/j.icarus.2007.12.009

Fassett, C. I., & Thomson, B. J. (2014). Crater degradation on the lunar maria: Topographic diffusion and the rate of erosion on the Moon. *Journal of Geophysical Research: Planets*, *119*, 2255–2271. https://doi.org/10.1002/2014JE004698

Fergason, R. L., Kirk, R. L., Cushing, G., Galuzska, D. M., Golombek, M. P., Hare, T. M., et al. (2017). Analysis of local slopes at the InSight landing site on Mars. *Space Science Reviews*, *211*(1-4), 109–133. https://doi.org/10.1007/s11214-016-0292-x

Forsberg-Taylor, N. K., Howard, A. D., & Craddock, R. A. (2004). Crater degradation in the Martian highlands: Morphometric analysis of the Sinus Sabaeus region and simulation modeling suggest fluvial processes. *Journal of Geophysical Research*, *109*, E05002. https://doi.org/10.1029/2004JE002242

Ganti, V., von Hagke, C., Scherler, D., Lamb, M. P., Fischer, W. W., & Avouac, J. P. (2016). Time scale bias in erosion rates of glaciated landscapes. *Science Advances*, *2*(10). https://doi.org/10.1126/sciadv.1600204

Gardner, T. W., Jorgensen, D. W., Shuman, C., & Lemieux, C. R. (1987). Geomorphic and tectonic process rates: Effects of measured time interval. *Geology*, *15*(3), 259–261. https://doi.org/10.1130/0091-7613(1987)15<259:GATPRE>2.0.CO;2

Garvin, J. B., & Frawley, J. J. (1998). Geometric properties of Martian impact craters: Preliminary results from Mars Orbiter Laser Altimeter. *Geophysical Research Letters*, *25*, 4405–4408. https://doi.org/10.1029/1998GL900177

Garvin, J. B., Sakamoto, S. E. H., Schnetzler, C., & Frawley, J. J. (2003). Craters on Mars: Global geometric properties from gridded MOLA topography, paper presented at 6th international conference on Mars, California Institute of Technology, Pasadena, California, 20–25 July.

Gault, D. E., Quaide, W. L., & Oberbeck, V. R. (1968). Impact cratering mechanisms and structures. In B. M. French, & N. M. Short (Eds.), *Shock metamorphism of natural materials*, (pp. 87–99). Baltimore: Mono Book Corporation.

Golombek, M. P., Bloom, C., Wigton, N., & Warner, N. H. (2014). Constraints on the age of Corinto crater from mapping secondaries in Elysium Planitia on Mars, *45th Lunar Planet. Sci. Conf.*, Abstract 1470.

Golombek, M. P., & Bridges, N. T. (2000). Erosion rates on Mars and implications for climate change: Constraints from the Pathfinder landing site. *Journal of Geophysical Research*, *105*, 1841–1853. https://doi.org/10.1029/1999JE001043

Golombek, M. P., Crumpler, L. S., Grant, J. A., Greeley, R., Cabrol, N. A., Parker, T. J., et al. (2006). Geology of the Gusev cratered plains from the Spirit rover transverse. *Journal of Geophysical Research*, *111*, E02S07. https://doi.org/10.1029/2005JE002503

Golombek, M. P., Grant, J. A., Crumpler, L. S., Greeley, R., Arvidson, R. E., Bell, J. F. III, et al. (2006). Erosion rates at the Mars Exploration Rover landing sites and long-term climate change on Mars. *Journal of Geophysical Research*, *111*, E12S10. https://doi.org/10.1029/2006JE002754

Golombek, M. P., Haldemann, A. F. C., Simpson, R. A., Fergason, R. L., Putzig, N. E., Arvidson, R. E., et al. (2008). Ch. 21: Martian surface properties from joint analysis of orbital, Earth-based, and surface observations. In J. F. Bell, III (Ed.), *The Martian surface: Composition, mineralogy and physical properties* (pp. 468–497). Cambridge: Cambridge University Press. https://doi.org/10.1017/CBO9780511536076.022

Golombek, M. P., Kipp, D. M., Warner, N. H., Daubar, I. J., Fergason, R. L., Kirk, R. L., et al. (2017). Selection of the InSight landing site. *Space Science Reviews*, *211*(1-4), 5–95. https://doi.org/10.1007/s11214-016-0321-9

Golombek, M. P., Robinson, K., McEwen, A. S., Bridges, N. T., Ivanov, B. A., Tornabene, L. L., & et al. (2010). Constraints on ripple migration at Meridiani Planum from Opportunity and HiRISE observations of fresh craters. *Journal of Geophysical Research*, *115*, E00F08. https://doi.org/10.1029/2010JE003628

Golombek, M. P., Warner, N. H., Ganti, V., Lamb, M. P., Parker, T. J., Fergason, R. L., & et al. (2014). Small crater modification on Meridiani Planum and implications for erosion rates and climate change on Mars. *Journal of Geophysical Research: Planets*, *119*, 2522–2547. https://doi.org/10.1002/2014JE004658

Grant, J. A., Arvidson, R. E., Bell, J. F. III, Cabrol, N. A., Carr, M. H., Christensen, P. R., et al. (2004). Surficial deposits at Gusev crater along Spirit rover traverses. *Science*, *305*(5685), 807–810. https://doi.org/10.1126/science.1099849

Grant, J. A., Arvidson, R. E., Crumpler, L. S., Golombek, M. P., Hahn, B., Haldemann, A. F. C., et al. (2006). Crater gradation in Gusev crater and Meridiani Planum, Mars. *Journal of Geophysical Research*, *111*, E02S08. https://doi.org/10.1029/2005JE002465

Greeley, R., & Schneid, B. D. (1991). Magma generation on Mars: Amounts, rates, and comparisons with Earth, Moon, and Venus. *Science*, *254*(5034), 996–998. https://doi.org/10.1126/science.254.5034.996

Hartmann, W. K. (2005). Martian cratering 8: Isochron refinement and the chronology of Mars. *Icarus*, *174*(2), 294–320. https://doi.org/10.1016/j.icarus.2004.11.023

Hartmann, W. K., Anguita, J., de la Casa, M. A., Berman, D. C., & Ryan, E. V. (2001). Martian Cratering 7: The role of impact gardening. *Icarus*, *149*, 37–53.

Hartmann, W. K., Malin, M., McEwen, A. S., Carr, M. H., Soderblom, L. A., Thomas, P. C., et al. (1999). Evidence for recent volcanism on Mars from crater counts. *Nature*, *397*(6720), 586–589. https://doi.org/10.1038/17545

Hartmann, W. K., & Neukum, G. (2001). Cratering chronology and the evolution of Mars. *Space Science Reviews*, *96*(1–4), 165–194. https://doi.org/10.1023/A:1011945222010

Head, J. W., Kreslavsky, M. A., & Pratt, S. (2002). Northern lowlands of Mars: Evidence for widespread volcanic flooding and tectonic deformation in the Hesperian period. *Journal of Geophysical Research*, *107*(E1), 5003. https://doi.org/10.1029/2000JE001445

Howard, A. D., Moore, J. M., & Irwin, R. P. III (2005). An intense terminal epoch of widespread fluvial activity on Mars: 1. Valley network incision and associated deposits. *Journal of Geophysical Research*, *110*, E12S14. https://doi.org/10.1029/2005JE002459

Hundal, C. B., Golombek, M. P., & Daubar, I. J. (2017). Chronology of fresh rayed craters in Elysium Planitia, Mars, *48th Lunar Planet. Sci. Conf.*, Abstract 1726.

Hynek, B. M., & Phillips, R. J. (2001). Evidence for extensive denudation of the Martian highlands. *Geology*, *29*(5), 407–410. https://doi.org/10.1130/0091-7613(2001)029<0407:EFEDOT>2.0.CO;2

Irwin, R. P. III, Howard, A. D., Craddock, R. A., & Moore, J. M. (2005). An intense terminal epoch of widespread fluvial activity on early Mars: 2. Increased runoff and paleolake development. *Journal of Geophysical Research*, *110*, E12S15. https://doi.org/10.1029/2005JE002460

Irwin, R. P. III, Tanaka, K. L., & Robbins, S. J. (2013). Distribution of Early, Middle, and Late Noachian cratered surfaces in the Martian highlands: Implications for resurfacing events and processes. *Journal of Geophysical Research: Planets*, *118*, 278–291. https://doi.org/10.1002/jgre.20053

Ivanov, B. A. (2001). Mars/Moon cratering rate ratio estimates. *Space Science Reviews*, *96*(1–4), 87–104. https://doi.org/10.1023/A:1011941121102

Judson, S., & Ritter, D. F. (1964). Rates of regional denudation in the United States. *Journal of Geophysical Research*, *69*, 3395–3401. https://doi.org/10.1029/JZ069i016p03395

Kirchner, J. W., Finkel, R. C., Riebe, C. S., Granger, D. E., Clayton, J. L., King, J. G., & et al. (2001). Mountain erosion over 10 yr, 10 k.y., and 10 m.y. time scales. *Geology*, *29*(7), 591–594. https://doi.org/10.1130/0091-7613(2001)029<0591:MEOYKY>2.0.CO;2

Kirk, R. L., Howington-Kraus, E., Rosiek, M. R., Anderson, J. A., Archinal, B. A., Becker, K. J., et al. (2008). Ultrahigh resolution topographic mapping of Mars with MRO HiRISE stereo images: Meter-scale slopes of candidate Phoenix landing sites. *Journal of Geophysical Research*, *113*, E00A24. https://doi.org/10.1029/2007JE003000

Mangold, N., Adeli, S., Conway, S., Ansan, V., & Langlais, B. (2012). A chronology of early Mars climatic evolution from impact crater degradation. *Journal of Geophysical Research*, *117*, E04003. https://doi.org/10.1029/2011JE004005
Marchant, D. R., & Head, J. W. (2007). Antarctic Dry Valleys: Microclimate zonation, variable geomorphic processes, and implications for assessing climate change on Mars. *Icarus*, *192*(1), 187–222. https://doi.org/10.1016/j.icarus.2007.06.018
Martin, Y., & Church, M. (1997). Diffusion in landscape development models: On the nature of basic transport relations. *Earth Surface Processes and Landforms*, *22*(3), 273–279. https://doi.org/10.1002/(SICI)1096-9837(199703)22:3<273::AID-ESP755>3.0.CO;2-D
McEwen, A. S., Eliason, E. M., Bergstrom, J. W., Bridges, N. T., Hansen, C. J., Delamere, W. A., et al. (2007). Mars Reconnaissance Orbiter's High Resolution Imaging Science Experiment (HiRISE). *Journal of Geophysical Research*, *112*, E05S02. https://doi.org/10.1029/2005JE002605
McEwen, A. S., Preblich, B. S., Turtle, E. P., Artemieva, N. A., Golombek, M. P., Hurst, M., et al. (2005). The rayed crater Zunil and interpretations of small impact craters on Mars. *Icarus*, *176*(2), 351–381. https://doi.org/10.1016/j.icarus.2005.02.009
McGlynn, I. O., Fedo, C. M., & McSween, H. Y. Jr. (2011). Origin of basaltic soils at Gusev crater, Mars, by aeolian modification of impact-generated sediment. *Journal of Geophysical Research*, *116*, E00F22. https://doi.org/10.1029/2010JE003712
Melosh, H. J. (1989). *Impact Cratering: A Geologic Process* (pp. 76–85). London: Oxford University Press.
Michael, G. G. (2013). Planetary surface dating from crater size-frequency distribution measurements: Multiple resurfacing episodes and differential isochron fitting. *Icarus*, *226*(1), 885–890. https://doi.org/10.1016/j.icarus.2013.07.004
Michael, G. G., & Neukum, G. (2010). Planetary surface dating from crater size-frequency distribution measurements: Partial resurfacing events and statistical age uncertainty. *Earth and Planetary Science Letters*, *294*(3–4), 223–229. https://doi.org/10.1016/j.epsl.2009.12.041
Mizutani, H., Kawakami, S., Takagi, Y., Kato, M., & Kumazawa, M. (1983). Cratering experiments in sands and a trial for general scaling law. *Journal of Geophysical Research*, *88*, A835–A845. https://doi.org/10.1029/JB088iS02p0A835
Moore, H. J. (1971). Large blocks around lunar craters. In *Analysis of Apollo 10 photography and visual observations*, *NASA Spec. Publ.*, (Vol. SP-232, pp. 26–27). Washington, DC: U.S. Government Printing Office.
Nelson, D. M., & Greeley, R. (1999). Geology of Xanthe Terra outflow channels and the Mars Pathfinder landing site. *Journal of Geophysical Research*, *104*, 8653–8669. https://doi.org/10.1029/98JE01900
Oberbeck, V. R., & Quaide, W. L. (1967). Estimated thickness of a fragmental surface layer of Oceanus Procellarum. *Journal of Geophysical Research*, *72*, 4697–4704. https://doi.org/10.1029/JZ072i018p04697
Pelletier, J. D., & Cline, M. L. (2007). Nonlinear slope-dependent sediment transport in cinder cone evolution. *Geology*, *35*(12), 1067–1070. https://doi.org/10.1130/G23992A.1
Phillips, R. J., Zuber, M. T., Solomon, S. C., Golombek, M. P., Jakosky, B. M., Banerdt, W. B., et al. (2001). Ancient geodynamics and global-scale hydrology on Mars. *Science*, *291*(5513), 2587–2591. https://doi.org/10.1126/science.1058701
Pike, R. J. (1974). Depth/diameter relations of fresh lunar craters: Revision from spacecraft data. *Geophysical Research Letters*, *1*, 291–294. https://doi.org/10.1029/GL001i007p00291
Pike, R. J. (1977). Size-dependence in the shape of fresh impact craters on the moon. In D. J. Roddy & R. B. Merrill (Eds.), *Impact and explosion cratering* (pp. 489–507). New York: Pergamon Press.
Pike, R. J. (1980). Control of crater morphology by gravity and target type: Mars, Earth, Moon. *Proceedings of the Lunar and Planetary Science Conference*, *11*, 2159–2189.
Pike, W. T., Staufer, U., Hecht, M. H., Goetz, W., Parrat, D., Sykulska-Lawrence, H., et al. (2011). Quantification of the dry history of the Martian soil inferred from in situ microscopy. *Geophysical Research Letters*, *38*, L24201. https://doi.org/10.1029/2011GL049896
Portenga, E. W., & Bierman, P. R. (2011). Understanding Earth's eroding surface with ^{10}Be. *Geological Society of America Today*, *21*(8), 4–10. https://doi.org/10.1130/G111A.1
Quaide, W. L., & Oberbeck, V. R. (1968). Thickness determinations of the lunar surface layer from lunar impact craters. *Journal of Geophysical Research*, *73*, 5247–5270. https://doi.org/10.1029/JB073i016p05247
Reiss, D., & Lorenz, R. D. (2016). Dust devil track survey at Elysium Planitia, Mars: Implications for the InSight landing sites. *Icarus*, *266*, 315–330. https://doi.org/10.1016/j.icarus.2015.11.012
Robbins, S. J., & Hynek, B. M. (2012). A new global database of Mars impact craters ≥1 km: 2. Global crater properties and regional variations of the simple-to-complex transition diameter. *Journal of Geophysical Research*, *117*, E06001. https://doi.org/10.1029/2011JE003967
Sadler, P. M. (1981). Sediment accumulation rates and the completeness of stratigraphic sections. *Journal of Geology*, *89*, 569–584.
Sadler, P. M. (1999). The influence of hiatuses on sediment accumulation rates. In P. Bruns & H. C. Haas (Eds.), *On the determination of sediment accumulation rates, GeoResearch Forum5* (pp. 15–40). Switzerland: Trans. Tech. Pub.
Sadler, P. M., & Jerolmack, D. J. (2014). Scaling laws for aggradation, denudation and progradation rates: The case for time-scale invariance at sediment sources and sinks. *Geological Society of London, Special Publication*, *404*, 69–88.
Saunders, I., & Young, A. (1983). Rates of surface processes on slopes, slope retreat and denudation. *Earth Surface Processes and Landforms*, *8*(5), 473–501. https://doi.org/10.1002/esp.3290080508
Scott, D. H., & Carr, M. H. (1978). Geologic map of Mars, U.S. Geol. Surv. Misc. Invest. Ser. Map, I-1083.
Senft, L. E., & Stewart, S. T. (2007). Modeling impact cratering in layered surfaces. *Journal of Geophysical Research*, *112*, E11002. https://doi.org/10.1029/2007JE002894
Soderblom, L. A., Condit, C. D., West, R. A., Herman, B. M., & Kreidler, T. J. (1974). Martian planetwide crater distributions: Implications for geologic history and surface processes. *Icarus*, *22*(3), 239–263. https://doi.org/10.1016/0019-1035(74)90175-4
Stewart, S. T., & Valiant, G. J. (2006). Martian subsurface properties and crater formation processes inferred from fresh impact crater geometries. *Meteoritics and Planetary Science*, *41*(10), 1509–1537. https://doi.org/10.1111/j.1945-5100.2006.tb00433.x
Stopar, J. D., Robinson, M. S., Barnouin, O., McEwen, A. S., Speyerer, E. J., Henriksen, M. R., & et al. (2017). Relative depths of simple craters and the nature of the lunar regolith. *Icarus*, *298*, 34–48. https://doi.org/10.1016/j.icarus.2017.05.022
Sweeney, J., Warner, N. H., Golombek, M. P., Kirk, R. L., Fergason, R. L., & Pivarunas, A. (2016). Crater degradation and surface erosion rates at the InSight landing site, western Elysium Planitia, Mars, *47th Lunar Planet. Sci. Conf.*, Abstract 1576.
Tanaka, K. L. (1986). The stratigraphy of Mars. *Journal of Geophysical Research*, *91*, E139–E158. https://doi.org/10.1029/JB091iB13p0E139
Tanaka, K. L., Skinner, J. A., & Hare, T. M. (2005). Geologic map of the northern plains of Mars, U.S. Geol. Surv. Misc. Invest. Ser. Map, 2888.
Tanaka, K. L., Skinner, J. A., Jr., Dohm, J. M., Irwin, R. P. III, Kolb, E. J., Fortezzo, C. M., et al. (2014). Geologic map of Mars, U.S. Geol. Surv. Sci. Invest. Map, 3292.
Tornabene, L. L., Watters, W. A., Osinski, G. R., Boyce, J. M., Harrison, T. N., Ling, V., & et al. (2018). A depth versus diameter scaling relationship for the best-preserved melt-bearing complex craters on Mars. *Icarus*, *299*, 68–83. https://doi.org/10.1016/j.icarus.2017.07.003
Warner, N. H., Golombek, M. P., Sweeney, J., Fergason, R. L., Kirk, R. L., & Schwartz, C. (2017). Near surface stratigraphy and regolith production in southwestern Elysium Planitia, Mars: Implications for Hesperian-Amazonian terrains and the InSight lander mission. *Space Science Reviews*, *211*(1-4), 147–190. https://doi.org/10.1007/s11214-017-0352-x

Warner, N. H., Gupta, S., Calef, F. J., Grindrod, P., & Goddard, K. (2015). Minimum effective area for high resolution crater counting of Martian terrains. *Icarus*, *245*, 198–240. https://doi.org/10.1016/j.icarus.2014.09.024

Warner, N. H., Gupta, S., Lin, S.-Y., Kim, J.-R., Muller, J.-P., & Morley, J. (2010). Late Noachian to Hesperian climate change on Mars: Evidence of episodic warming from transient crater lakes near Ares Vallis. *Journal of Geophysical Research*, *115*, E06013. https://doi.org/10.1029/2009JE003522

Warner, N. H., Gupta, S., Muller, J.-P., Kim, J.-R., & Lin, S.-Y. (2009). A refined chronology of catastrophic outflow events in Ares Vallis, Mars. *Earth and Planetary Science Letters*, *288*(1-2), 58–69. https://doi.org/10.1016/j.epsl.2009.09.008

Watters, W. A., Geiger, L. M., Fendrock, M. A., & Gibson, R. (2015). Morphometry of small recent impact craters on Mars: Size and terrain dependence, short-term modification. *Journal of Geophysical Research: Planets*, *120*, 226–254. https://doi.org/10.1002/2014JE004630

Watters, W. A., Hundal, C. B., Radford, A., Collins, G. S., & Tornabene, L. L. (2017). Dependence of secondary crater characteristics on down-range distance: High-resolution morphometry simulations. *Journal of Geophysical Research: Planets*, *122*, 1773–1800. https://doi.org/10.1002/2017JE005295

Werner, S. C., & Tanaka, K. L. (2011). Redefinition of the crater-density and absolute-age boundaries for the chronostratigraphic system of Mars. *Icarus*, *215*(2), 603–607. https://doi.org/10.1016/j.icarus.2011.07.024

Wilcox, B. B., Robinson, M. S., Thomas, P. C., & Hawke, B. R. (2005). Constraints on the depth and variability of the lunar regolith. *Meteoritics and Planetary Science*, *40*(5), 695–710. https://doi.org/10.1111/j.1945-5100.2005.tb00974

Xie, M., Zhu, M.-H., Xiao, Z., Wu, Y., & Zu, A. (2017). Effect of topography degradation on crater size-frequency distributions: Implications for populations of small craters and age dating. *Geophysical Research Letters*, *44*, 10,171–10,179. https://doi.org/10.1002/2017GL075298

Erratum

In the originally published version of this article, the contribution list was incorrect. The correct contributions are as follows:

Conceptualization: N. H. Warner, M. P. Golombek
Data Curation: N. H. Warner, J. Sweeney
Formal Analysis: J. Sweeney, N. H. Warner, V. Ganti, M. P. Golombek
Investigation: J. Sweeney, N. H. Warner, V. Ganti, M. P. Golombek, M. P. Lamb
Methodology: N. H. Warner, J. Sweeney, V. Ganti, R. Fergason, R. Kirk
Resources: N. H. Warner, M. P. Golombek, V. Ganti, R. Fergason, R. Kirk
Validation: N. H. Warner, M. P. Golombek, V. Ganti, R. Fergason, M. P. Lamb
Visualization: N. H. Warner, J. Sweeney, V. Ganti
Writing - original draft: J. Sweeney, N. H. Warner, V. Ganti

This error has since been corrected and this version may be considered the authoritative version of record.